

Interchain interactions, multimagnon condensation, and strain effect in the chain compound NaVOPO₄

Manoj Gupta^{✉,*}, Manodip Routh,^{*} Manoranjan Kumar^{✉,†} and Tanusri Saha Dasgupta^{✉,‡}

Department of Condensed Matter and Materials Physics, S. N. Bose National Centre for Basic Sciences, Kolkata 700106, India



(Received 11 March 2024; revised 1 July 2024; accepted 13 August 2024; published 26 August 2024)

Employing first-principles modeling and many-body methods, the magnetic properties of the spin-1/2 chain compound NaVOPO₄ are explored. The extensive first-principles calculations establish an intricate three-dimensionally-coupled model that consists of weakly alternating $J - J'$ antiferromagnetic chains running along criss-cross directions between two consecutive ab planes, connected via two subleading couplings: a ferromagnetic exchange along the c direction (J_c) and a weaker antiferromagnetic exchange (J_d) along the body-diagonal direction. The exact diagonalization and density matrix renormalized group study has been carried out on a two-dimensional spin model with $J - J' - J_c$ and effective J_d couplings, constructed based on the full model, for numerical ease. The $J_c - J_d$ phase diagram is found to host a *disorder* phase with a finite spin gap for comparable values of J_c and J_d , arising out of the competing nature of these two interactions, other than two ordered phases. The calculated thermodynamic properties of this model provide a fair description of experimentally measured data. The predominant manifestation of J_c and J_d in the disorder phase happens in the stabilization of a multimagnon condensed phase upon gap closing by application of an external magnetic field. We further explore the effect of tensile uniaxial strain, which is found to drive the system from a gapful to a gapless ground state.

DOI: [10.1103/PhysRevB.110.054441](https://doi.org/10.1103/PhysRevB.110.054441)

I. INTRODUCTION

Over the years, one-dimensional antiferromagnetic $S = 1/2$ chain compounds have attracted the interest of researchers. They offer a fascinating playground to study properties such as spin-gap states, spin-charge separation, and quantum criticality, dictated by the quantum fluctuation effect arising from the low dimensionality and smallness of spin [1–4]. Many of these one-dimensional spin compounds host a spin gap in the spin excitation spectra between the singlet ground state and the triplet excited state, which may arise from different competing exchanges. As expected, these spin chains with spin gaps are sensitive to perturbations such as subleading interchain interactions, strain, and/or external magnetic field. In particular, the spin gap can be reduced or even closed by applying an external field above a threshold value, which leads to the emergence of a multitude of field-induced phases [5–10].

In this context, the family of vanadate compounds with V^{4+} ions separated by PO₄ or AsO₄ tetrahedral units have drawn attention in recent time [11–14]. Among them, in the present study, we focus on NaVOPO₄ (NVOPO). Although this compound was synthesized in the early 1990s [15,16], there is a renewed interest due to the possible realization of a spin-1/2 chain system [14] as well as for its potential use as cathode material [17]. Low-temperature x-ray diffraction

measurements rule out possible Peierls transition [14]. The magnetic susceptibility data [14] confirm the nominal 4^+ valence of V, with $S = 1/2$ spin, and dominance of antiferromagnetic coupling. The magnetic susceptibility data could be fitted with an alternating-chain spin model with an extremely weak alternation parameter close to 1, suggesting the compound may be at the boundary of the uniform chain and the alternating-chain model. Magnetization isotherm measurement [14] established the existence of a spin gap with the critical field of gap closing ≤ 2 T leading to a possible Bose-Einstein condensed (BEC) phase [18–21] at low temperature. The absence of long-range order in the absence of an external magnetic field was further confirmed in NMR measurements [14]. While the above observations support the spin-gapped ground state of NVOPO and an external field-driven possible condensed phase, the detailed analysis of the underlying spin model and its implication have not been explored. The theoretical modeling reported in the same work [14] finds evidence of subleading interchain interactions. However, the experimental results are interpreted as a bond-alternating spin chain model with an extremely weak alternation parameter of 0.98 and negligible interchain couplings. The issue of interchain interactions thus remains unresolved.

The simple fitting treatment to magnetic susceptibility data, as often adapted, makes it hard to predict details of the microscopic model. Such a model would typically involve the prediction of exchange paths and the relative magnitudes of various magnetic interactions. This in turn calls for a microscopic investigation in terms of *ab initio* calculations to derive the underlying spin model coupled with many-body methods for calculation of magnetic properties. Very often,

*These authors contributed equally to this work.

†Contact author: manoranjan.kumar@bose.res.in

‡Contact author: t.sahadasgupta@gmail.com

the true nature of the exchange networks in these compounds differs from the mere expectation from the crystal structure. A famous example in this context is that of $(\text{VO})_2\text{P}_2\text{O}_7$ [22], which turns out to be an alternating spin chain compound while originally it was thought of as a two-leg spin ladder system based on structural considerations.

In this study, we thus revisit the modeling of the compound through rigorous and extensive density functional theory (DFT) calculations. Our calculations are based on the construction of a three-orbital, low-energy Wannier Hamiltonian and solution of total energy calculations of a large number of equations, to rule out the dependency of the derived model on the chosen spin configurations. This rigorous study established a robust nature of intrachain couplings with an alternation ratio of 0.92 as opposed to 0.98 as predicted from susceptibility fit [14]. Most importantly, this investigation resulted in two additional subleading interchain interactions, the values of which are found to depend strongly on the chosen spin configurations. Employing the exact diagonalization and density matrix renormalization group study of a DFT-inspired model spin Hamiltonian, we establish the important contribution of these subleading interactions in introducing *frustration* in the system, in terms of the competing nature of these interactions. We map out an intriguing phase diagram in the phase space of subleading interchain interactions, rationalized by large variations in their values in first-principles estimates. Due to the competing nature, interestingly at the point when the two subleading terms become equal, thereby compensating each other, the spin gap value can be described by a single alternating chain model. The gap value reduces in moving away from the compensation point, finally leading to ordered states when one subleading term becomes substantial and completely dominates the other. These competing subleading interactions, however, manifest themselves in the excited-state properties upon gap closing by the application of an external magnetic field, and a multimagnon condensed phase [23–30] is observed. Importantly, at the compensation point, although the gap value can be mimicked by a single alternating chain model, the same model will fail to describe the multimagnon condensed phase. We compute different thermodynamic properties and compare them with experimental measurements. We demonstrate the goodness of the model with subleading interactions in capturing the experimental data. We further explore the effect of strain. The introduction of a moderate amount of uniaxial strain is found to tune the subleading interactions, driving a strain-assisted quantum transition from gapful to a gapless phase. Our prediction may be verified in future experiments. The 2D spin model introduced in this study, inspired by the NVOPO physics, will be of general interest in study of frustrated magnets.

II. METHOD

The first-principles DFT calculations were carried out in two different basis sets: (a) a pseudopotential, plane-wave basis, and (b) a muffin-tin orbital basis. The consistency of the two different basis-set calculations has been cross-checked in terms of band structure and density of state plots. The construction of a low-energy Hamiltonian was achieved in a

muffin-tin orbital basis, while for accurate total energy calculations and structural relaxation, a plane-wave basis was used.

The plane-wave calculations were carried out employing projector augmented-wave potential [31], as implemented in the Vienna Ab-initio Simulation package [32–34]. The convergence of energies and forces was ensured by using a plane-wave energy cutoff of 600 eV and Brillouin zone (BZ) sampling with $6 \times 6 \times 6$ Monkhorst-Pack grids. During the structural relaxation, the ions were allowed to move until the atomic forces became lower than $0.0001 \text{ eV}/\text{\AA}$.

The Perdew-Burke-Ernzerhof generalized gradient approximation (GGA) [31] was used to approximate the exchange-correlation functional. To check the influence of the correlation effect at the transition-metal site, beyond GGA, GGA+ U with supplemented Hubbard U correction was carried out [35].

The muffin-tin orbital (MTO) basis was used in deriving a low-energy, few-band Hamiltonian in the effective t_{2g} Wannier basis of the transition-metal ions. For this purpose, the NMTO-downfolding technique [36] of integrating out degrees of freedom that are not of interest, starting from the all-orbital DFT band-structure, was employed. The self-consistent potentials required for these calculations were generated through Stuttgart implementation of the linear-MTO (LMTO) package [37]. For muffin-tin orbital calculations, the MT radii were chosen as 1.89, 1.25, 1.161, and 0.86 \AA for Na, V, P, and O, respectively.

State-of-the-art numerical techniques of ED [38–40] and DMRG [41–43] were used to solve the DFT-derived spin model. While for small system sizes, ED was used, for larger system sizes the DMRG method of systematic truncation of irrelevant degrees of freedom and renormalization of coupling parameters for growing the system sizes was used. The accuracy in DMRG is known to decrease for systems with long bonds or multiple times renormalized operators used in the construction of the Hamiltonian. To reduce the number of multiple times renormalized operators used in the Hamiltonian, a four-new-site algorithm is used. It demonstrates better convergence in the $J - J'$ model with the same computational cost [44]. In particular, in the present work, we used this modified DMRG method [44] on a rectangular lattice with cylindrical geometry. Cylinders are labeled XC or YC, corresponding to open boundary conditions (OBCs) along the larger lattice direction (X-direction) and periodic boundary conditions (PBCs) along the smaller direction (Y-direction). We retain up to $m = 700$ density matrix eigenstates during the renormalization process. We perform ~ 10 – 12 sweeps until the ground-state energy converges within an error of $\sim 10^{-5} \text{ J}$.

III. CRYSTAL STRUCTURE

The NaVOPO_4 compound crystallizes in the monoclinic structure with $P21/c$ (no. 14) space group and $Z = 4$. Starting from the experimentally determined crystal structure [14], for an accurate determination of the positions of light atoms such as O, we optimize the structure, keeping the lattice parameters as well as high-symmetry atomic positions fixed, under the selective dynamics scheme. In the optimized geometry, the magnetic ion in the structure, V^{4+} , is surrounded by six

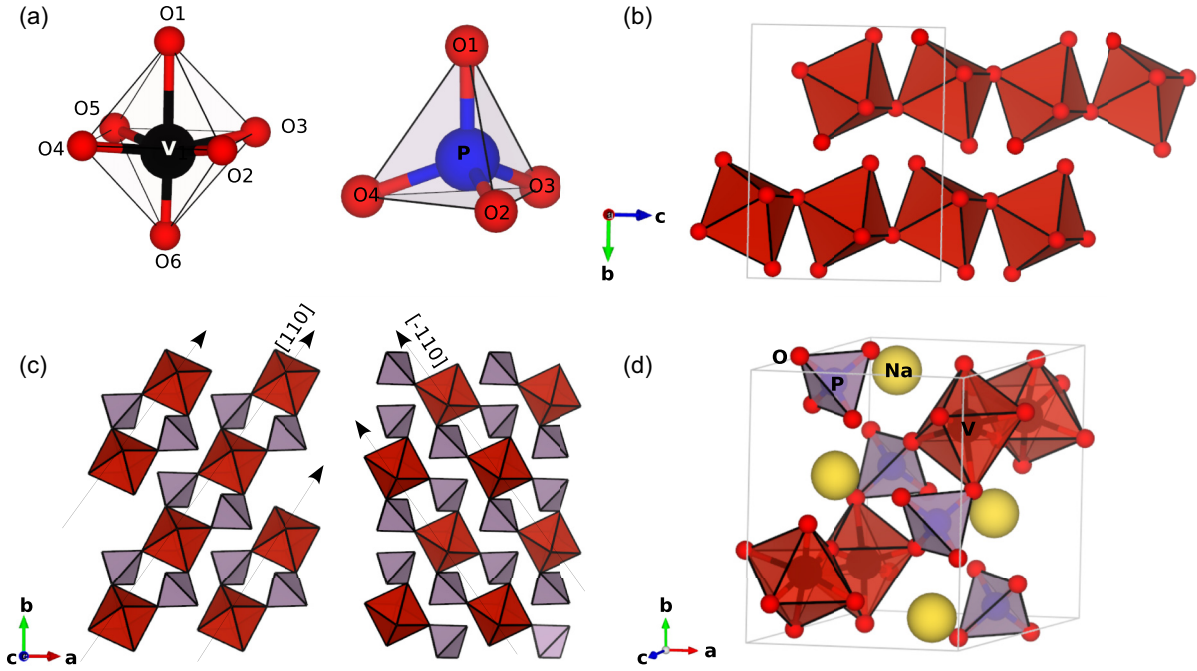


FIG. 1. Crystal structure of NaVOPO₄. (a) Structural units of distorted VO₆ octahedra surrounded by six inequivalent oxygen atoms (O1–O6) and PO₄ square pyramid formed by O1–O4 inequivalent oxygen atoms. (b) Corned-shared VO₆ octahedra forming structural chains along the crystallographic *c* axis. The rectangular box represents the unit cell. (c) VO₆ octahedra connected by a pair of PO₄ square forming VO₆-PO₄-PO₄-VO₆ chains running along [110] and $\bar{1}\bar{1}0$ in two consecutive *ab* layers. (d) Three-dimensional network formed by criss-cross running chains and Na atoms.

inequivalent oxygen atoms (O1–O6) with four equatorial V–O bonds in the range 1.98–2.01 Å, and one long and one short apical bond of length 2.13 and 1.62 Å, respectively. This results in a distorted VO₆ octahedron of C_{2h} symmetry, instead of O_h symmetry of an ideal octahedra. The P⁵⁺ ions, on the other hand, form a nearly regular PO₄ tetrahedron with P–O bond lengths of ~ 1.54 Å [cf. Fig. 1(a)]. The corner-shared VO₆ octahedra form structural chains, running along the crystallographic *c*-axis, as shown in Fig. 1(b). A pair of VO₆ octahedra bridged by a pair of PO₄ tetrahedra also form chains running along [110] and $[-110]$ axes in two consecutive *ab* plane, as shown in Fig. 1(c). A three-dimensional criss-cross connected network is formed by corner sharing of VO₆ octahedra and PO₄ tetrahedra, in which Na⁺ ions sit in the hollows to bring cohesion in the structure, as shown in Fig. 1(d).

IV. DFT ESSENTIALS

A. Basic electronic structure

The non-spin-polarized GGA-PBE density of states (DOS) of NVOPO, projected onto V- d_{xy} , d_{yz} , d_{xz} , $d_{x^2-y^2}$, and $d_{3z^2-r^2}$ orbital characters, is shown in Fig. 2(a). The local coordinate system is chosen with the local *z*-axis and *x*-axis pointing along V–O6 and approximately along the V–O3 bond, respectively. Following the nominal d^1 valence of the V⁴⁺ ion, the V-*d* states are found to be mostly unfilled, with 1/6 of the states being filled. The crystal-field splitting of the V-*d* states computed from the real-space representation of the V-*d*-only Hamiltonian obtained from NMTO-downfolding calculations

by integrating all other degrees of freedom is shown in the inset of Fig. 2(a). As is seen, the octahedral environment pushes the $d_{x^2-y^2}$ and $d_{3z^2-r^2}$ levels, belonging to the e_g manifold 2–3 eV away from the d_{xy} , d_{yz} , d_{xz} levels, forming the t_{2g} manifold. The octahedral distortion leads to further splitting of about 1 eV between $d_{x^2-y^2}$ and $d_{3z^2-r^2}$ and 0.7–0.8 eV between d_{xy} and d_{yz}/d_{xz} along with a tiny splitting between d_{yz} and d_{xz} . The crystal-field splitting between d_{xy} and d_{yz}/d_{xz} being smaller than the dispersional width associated with d_{xy} , d_{yz} , and d_{xz} , the t_{2g} manifold consisting of 12 bands arising out of 4 V ions in the unit cell [cf. Fig. 2(b)] crosses the Fermi level (E_F), separated from the e_g manifold by about 0.5 eV. The metallic nature of the GGA-PBE non-spin-polarized electronic structure, contrary to the insulating character of the compounds, suggests the inadequacies of the GGA to capture the strong correlation effect at the V site. Inclusion of Hubbard correction (U), within the GGA calculation supplemented with U (GGA+ U), pushes the d_{xy} bands below E_F , well separated from other t_{2g} bands, opening a gap at E_F . See the Supplemental Material (SM) [45]. The non-spin-polarized GGA electronic structure, however, serves as a good starting point for identifying the predominant V–V hopping pathways in a low-energy representation of the problem that is responsible for the magnetic exchanges.

Although the basic GGA electronic structure shows an overall similarity with the LDA electronic structure of one of the related compounds, AgVOAsO₄, studied in past literature [11] in terms of the presence of partially filled low-lying d_{xy} bands strongly hybridizing with higher-lying d_{yz}/d_{xz} bands, there are subtle differences in terms of crystal-field splittings

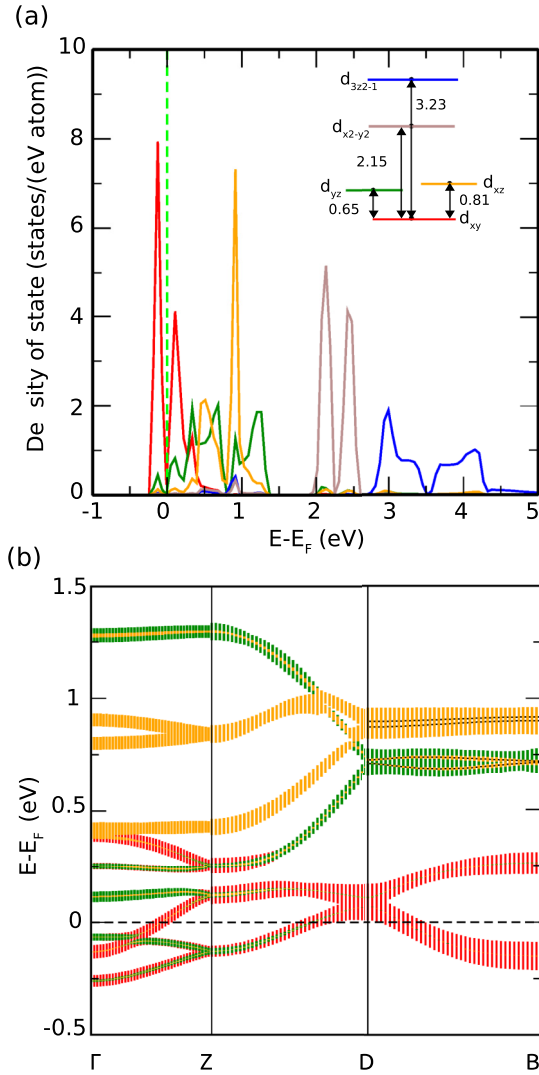


FIG. 2. The non-spin-polarized GGA density of states and band structure of NVOPO. (a) Density of states, projected to different V- d characters, d_{xy} (red), d_{yz} (green), d_{xz} (orange), d_{x2-y2} (brown), and d_{3z2-y2} (blue). Zero of the energy is set at E_F . Inset shows the crystal-field splitting (in eV) of the V- d levels. (b) Orbital projected band structure, plotted in an energy range close to E_F . Fatness of the bands denotes the associated orbital character (d_{xy} , red; d_{yz} , green; and d_{xz} , orange).

and bandwidths, which are expected to bring about crucial differences in the spin model of the two compounds.

B. Low-energy Hamiltonian and effective V-V exchange pathways

In an attempt to derive a V- d -only low-energy Hamiltonian from DFT calculations, we resort to the energy-selective N th-order muffin-tin orbital-based (NMTO-based) downfolding technique [36]. Starting from a self-consistent DFT calculation in the linear muffin-tin orbital basis [37], an NMTO-downfolding calculation arrives at a low-energy V- d Hamiltonian by integrating out degrees that are not of interest. This defines effective V Wannier functions with the head of the function shaped as V- d orbital characters, and tails shaped

as integrated-out orbitals having appreciable hybridization with V- d .

To construct the low-energy model of NVOPO, we consider a three-orbital model in which V- d_{xy} , d_{yz} , and d_{xz} are kept active, and all the rest, Na- s , O- p , P- p , as well as V- e_g degrees of freedom, are integrated out. Construction of a three-orbital t_{2g} -only model is justifiable because the DFT-estimated $t_{2g} - e_g$ crystal field of 2–3 eV gets renormalized to 4–5 eV upon application of the missing correlation effect (see the SM [45]), which would weaken the $t_{2g} - e_g$ hybridization. A very similar approach was also adopted in Ref. [11] for modeling AgVOAsO₄.

We would like to stress that, in contrast to the DFT results of Ref. [14] in which a d_{xy} -only model was proposed, we find that such a one-orbital description does not work satisfactorily due to strong hybridization between three t_{2g} 's and the entangled nature of these bands.

The three-orbital downfolded band structure provides a faithful representation of the DFT bands, as shown in Fig. 3(a). The real-space representation of the three-orbital model leads to 3×3 on-site and hopping matrices joining the two V sites with a connecting vector. The detailed results are presented in Appendix A. The two leading hopping pathways appear to be V-V interactions through the PO₄ bridges, t and t' forming alternating chains running along the [110] and $[-110]$ directions in the ab planes, as shown in Figs. 3(b) and 3(c). The next subleading interactions appear to be between corner-shared VO₆ running along [001], t_c , and the V-V pairs in the body-diagonal positions connecting two ab planes, t_a , as shown in Figs. 3(d) and 3(e).

To understand the dominating effect of t and t' connecting V pairs with no shared O, over t_c between V's with corner shared connectivity, we plot the overlap of V effective Wannier functions, placed at 1NN and 3NN V sites [cf. Figs. 3(f) and 3(g)]. As is seen, for t_c , due to the tilted geometries of the octahedra and their corner-shared nature, the overlap of the two functions is minimal at the connecting O site. On the other hand, due to finite hybridization between O- p and P- p , the O- p like tails of Wannier functions bend and make a connection at the intervening P site for V pairs, separated by PO₄ bridges, resulting in a well-defined hopping path for t . This general aspect is found to be similar to that found for AgVOAsO₄ [11], although the details are different.

Starting from the information of the hopping integrals, a second-order perturbation theory can be employed to provide a rough estimate of the exchange integrals (J) in the limit of the Coulomb interaction U that is much larger than the hopping integrals. Considering the d_{xy} orbitals to be majorly half-filled and d_{xz}/d_{yz} orbitals to be majorly empty leads to (a) an antiferromagnetic interaction due to the hopping of an up-electron from an occupied d_{xy} state to a neighboring d_{xy} state, occupied by a down-electron, costing U amount of energy; and (b) a ferromagnetic interaction arising from electronic hopping from occupied d_{xy} to unoccupied d_{yz} , d_{xz} states, separated by charge-transfer energy of Δ , as shown in the schematic figure in the SM [45]. The latter process involves the energy gain between electrons in a parallel spin configuration by Hund's coupling (J_H). Thus the effective exchange interaction can be written following the formulation

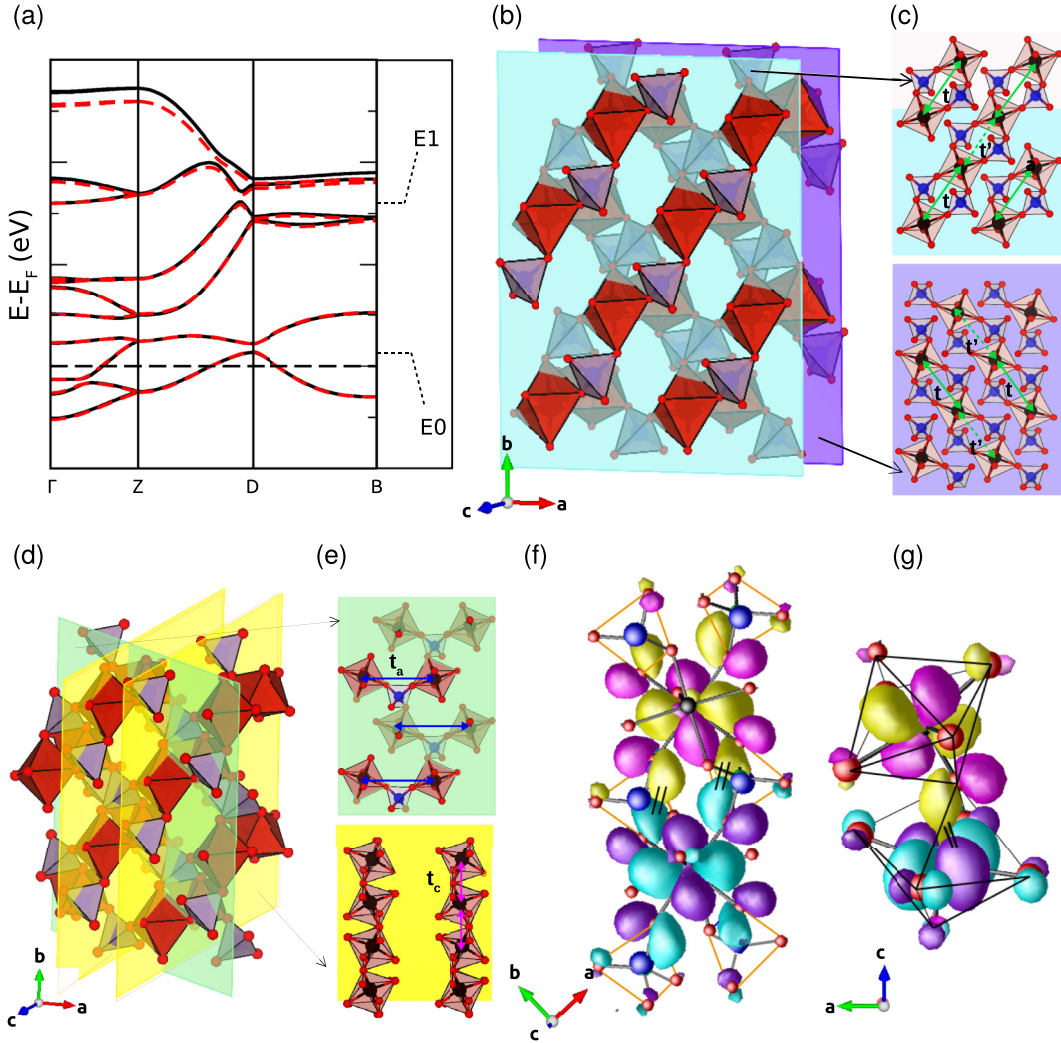


FIG. 3. Low-energy three-orbital model. (a) Downfolded band structure (dotted red lines) in comparison to full DFT band structure (solid black lines) plotted along the high-symmetry directions of monoclinic BZ. Zero of the energy is set at E_F . The energy points ($E0$ and $E1$) used for energy-selective NMTO-downfolding calculation have been marked. (b) and (c) The alternating chains of V ions, connected by hopping interactions t and t' . The blue and magenta shaded planes denote two successive ab planes. (d) and (e) V ions connected by t_c and t_a hoppings. Different ab and ac planes are shaded to highlight the complex connectivity. (f) Overlap of effective Wannier functions $d_{xy} - d_{xy}$ placed at neighboring V sites connected by hopping t . Shown are the constant value isosurfaces with lobes of opposite signs colored as magenta and yellow for one site and blue and purple for a neighboring site. (g) Same as (f) but between d_{xy} and d_{xz} placed at V sites connected through hopping t_c .

of Kugel-Khomskii [46], which has been applied successfully to several cases [11,47,48] as

$$J = J_{\text{AFM}} + J_{\text{FM}} = \frac{4t_{xy,xy}^2}{U} - \sum_{\alpha=xy, \beta=yz, xz} \frac{4t_{\alpha,\beta}^2 J_H}{(U + \Delta_{\alpha,\beta})(U + \Delta_{\alpha,\beta} - J_H)}. \quad (1)$$

In the above we have assumed that the intra-atomic Coulomb interaction and Hund's coupling do not depend on the particular orbital, i.e., the repulsion between different orbitals ($U_{mm'}$) is the same as that between the same orbital ($U_{mm} = U$, and $J_H^{mm'} = J_H$, where m and m' are orbital indices that run over the three t_{2g} orbitals).

The exchange interactions estimated employing the above formula, and using DFT inputs for Δ and $t_{\alpha,\beta}$'s with a

choice of $U = 4$ eV and $J_H = 1$ eV, are listed in Table II of Appendix A. This gives rise to the antiferromagnetic nature of the two dominating exchanges, J and J' , related to hopping integrals t and t' , two subleading exchanges, one of a ferromagnetic nature, J_c related to t_c , and another of an antiferromagnetic nature, J_a related to t_a .

C. Exchange Interactions from total energy calculations

The second-order perturbative formula employing DFT inputs of effective hopping integrals and on-site matrix elements, as discussed above, provides a rough estimate of the relative importance of different exchanges. This step, therefore, serves as an important step for the identification of the underlying spin model in the complex geometry of NVOPO. However, once this identification is done, in the next step

an accurate determination of exchanges is required. For this purpose, we employ the total energy method in which various J 's are evaluated by mapping the GGA+ U total energies of different possible spin configurations of V ions to an effective $J - J' - J_c - J_a$ spin Hamiltonian. As opposed to earlier calculations in this context [14], our total energy calculations are carried out by solving a large number of equations ($\sim 11C_4$) obtained from GGA+ U total calculations of 12 different spin configurations to avoid any bias on the chosen spin configurations. The details of the results are presented in Appendix B. Our rigorous analysis established a robust alternation ratio of 0.92 in comparison to 0.98 extracted from susceptibility fit [14]. The obtained alternation ratio, however, is in good agreement with the DFT value of 0.93, as reported in Ref. [14]. Our analysis, importantly, uncovered a strong dependency of the values of J_a and J_c on the chosen spin configurations. The AFM and FM nature of J_a and J_c , though, is maintained in each choice. Thus the subleading terms J_c and especially J_a show a large variation (cf. Table III in Appendix B).

V. SOLUTION OF THE SPIN-HAMILTONIAN

We employed the many-body techniques of exact diagonalization and density matrix renormalization group to solve the *ab initio* derived spin Hamiltonian. However, the three-dimensionally-coupled network of alternating chains poses a numerical challenge in solving the Hamiltonian, which may involve the application of complex numerical tools such as a functional renormalization group [49]. To make the problem numerically tractable, we consider a two-dimensional (2D) model that captures the essential features of the full 3D problem. Figures 4(a) and 4(b) show the full 3D model and the 2D model derived from the 3D model, respectively. See Appendix C for details. In the full model, a parallel array of $J - J'$ chains runs along two perpendicular directions, in two consecutive *ab* planes, stacked along the *c* direction, connected by J_c . In its two-dimensional projection, this is mapped onto the $J - J'$ chain, alternating with a uniform chain of average interaction $(J + J')/2$, connected via J_c . Furthermore, in order to capture the effect of J_a present on the body diagonal of the 3D Hamiltonian, an effective, renormalized interaction J_d , which is a combination of J_a and J_c , is considered on the phase diagonal of the 2D plane. While the projection establishes a 2D model of $J - J'$ chains that alternate with a uniform chain of average interaction $(J + J')/2$, connected via J_c (see Fig. 14 in Appendix C), the exact estimate of J_d is nontrivial, given the complex intricacy of the 3D model, as is evident from the 3D and 2D structures, presented in Fig. 15 of Appendix C. We thus approximate it as $J_a + \gamma J_c$, where γ is a variational parameter chosen to reproduce the correct ground state of NVOPO. It should be noted that both 3D and the constructed 2D models are frustrated, as demonstrated in Appendix C. J_a and J_c in the 3D model and J_d in the 2D model are primary factors for introducing the frustration in the system. In the 3D model this involves one FM and three AFM couplings of four bond units, and in the 2D model this involves two FM and one AFM coupling of three bond units. Thus, two main aspects are ensured in this construction: (i) the coordination number of each interaction is the same as in the full model, and (ii) the frustrated nature arising due to

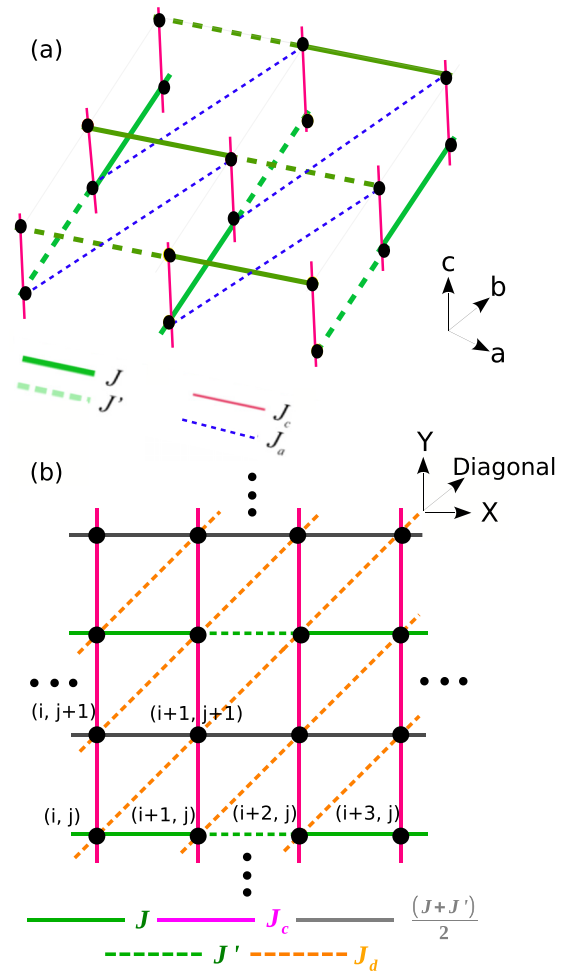


FIG. 4. (a) The 3D spin model of NVOPO, where solid green, dashed green, red, and dotted blue lines represent V-V magnetic exchanges, J , J' , J_c , and J_a , respectively. (b) Effective 2D spin model, with solid green, dashed green, black, and dashed orange representing J , J' , $\bar{J} = \frac{(J+J')}{2}$, and J_d interactions, respectively. While the exchanges J and J' are the same as in the 3D model, \bar{J} and J_d are effective interactions arising from 3D to 2D mapping. See the text and Appendix C for details.

competing antiferromagnetic and ferromagnetic interactions is kept intact.

The Hamiltonian for the 2D model of the spin-1/2 isotropic Heisenberg system in an axial magnetic field B is given by

$$\begin{aligned} \mathcal{H} = & \sum_{j=1,3,\dots}^{L_Y} \sum_{i=1}^{L_X} \left(J \vec{S}_{i,j} \cdot \vec{S}_{i+1,j} + J' \vec{S}_{i+1,j} \cdot \vec{S}_{i+2,j} \right. \\ & \left. + \frac{J+J'}{2} \vec{S}_{i,j+1} \cdot \vec{S}_{i+1,j+1} \right) \\ & + \sum_{j=1}^{L_Y} \sum_{i=1}^{L_X} \left(J_c \vec{S}_{i,j} \cdot \vec{S}_{i,j+1} + J_d \vec{S}_{i,j} \cdot \vec{S}_{i+1,j+1} - BS_{i,j}^z \right). \end{aligned} \quad (2)$$

$\vec{S}_{i,j}$ is the spin-1/2 operator at a site with coordinates (i, j) in a 2D geometry ($L_X \times L_Y$), as shown in Fig. 4(b). The first and second terms of the Hamiltonian represent the odd-numbered

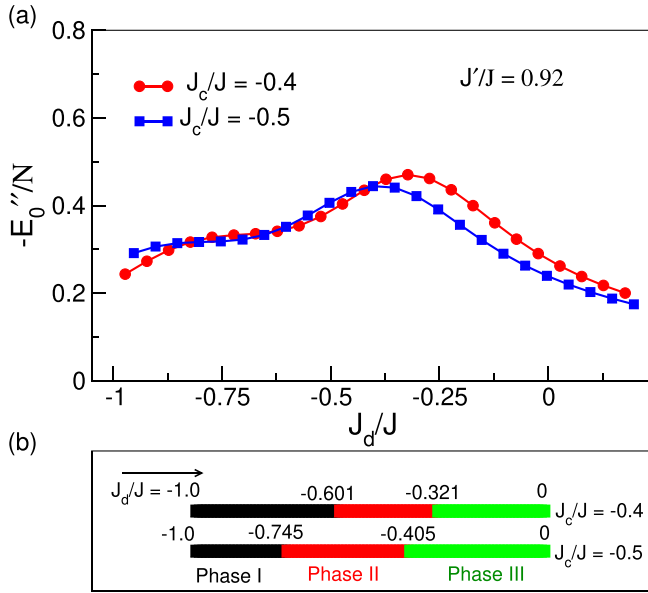


FIG. 5. (a) Second-order derivative of the ground-state energy per site, $-E''_0/N$, calculated from ED on a 24-site torus as a function of J_d/J for different J_c/J values. The two prominent peaks in $-E''_0/N$ serve as indicators of the phase boundaries separating phase I and phase II, and phase II and phase III, as shown in (b).

and even-numbered spin chains in the 2D plane, with alternating $J - J'$ antiferromagnetic exchanges and uniform antiferromagnetic exchanges, respectively. The third term represents the subleading competing ferromagnetic exchanges J_c along the Y-direction and J_d along the diagonal between spins on nearest-neighbor chains as shown in Fig. 4(b). The model exhibits a high degree of frustration due to ferromagnetic subleading exchanges J_c and J_d . Based on the inputs of *ab initio* calculations, in all subsequent calculations we fix the dominant exchange ratio J'/J to 0.92. Keeping in mind the large variation in J_c and J_d values with $|J_c|$ two to four times larger than $|J_d|$, the subleading exchange ratios J_c/J and J_d/J are varied within the ranges $-0.5 \leq J_c/J \leq 0$ and $-1 \leq J_d/J \leq 0$, respectively.

VI. QUANTUM PHASES AT $B = 0$

In this section, we study the ground-state (GS) properties of the Hamiltonian given in Eq. (2) in the J_c/J and J_d/J parameter space. To characterize the quantum phases and possible boundaries between them, we employ two numerical techniques: exact diagonalization (ED) and density matrix renormalization group (DMRG). The second derivative of energy $-E''/N$ was calculated from ED for a 24-site system, and spin correlations $C(r) = \langle \vec{S}_i \cdot \vec{S}_{i+r} \rangle$ in the GS were calculated from DMRG for relatively larger system sizes of 80–120 sites.

A. Second derivative of energy

The second derivative of the GS energy is expected to show maxima or discontinuity at the transition points between different phases, and it serves as an indicator of the existence of different phases. Figure 5(a) shows $-E''/N$ as a function of J_d/J for two representative values of $J_c/J = -0.4, -0.5$ with

a fixed value of $J'/J = 0.92$. A similar nature was found for $J_c/J = -0.1, -0.2, -0.3$ (not shown in the figure for clarity). The two maxima in $-E''/N$, as seen in the figure, suggest that there are three distinct phases. Figure 5(b) shows the transition points between three phases for $J_c/J = -0.4, -0.5$. We characterize these phases—phase I, phase II, and phase III—in the following section through spin correlations obtained from DMRG for larger system sizes.

B. Spin correlations $C(r)$

To further characterize the three phases found in ED, we have used DMRG to analyze the nature of the ground state of \mathcal{H} on cylindrical geometries, which is discussed in detail in Appendix D. We computed spin correlations in the three different phases identified in ED: (i) weak J_c , strong J_d (phase I: $J_c/J = -0.3, J_d/J = -0.8$); (ii) comparable J_d, J_c (phase II: $J_c/J = J_d/J = -0.3$); and (iii) strong J_c , weak J_d (phase III: $J_c/J = -0.5$ and $J_d/J = -0.1$). Since the Hamiltonian is isotropic, the correlations S^x, S^y , and S^z are identical. We computed the total correlation, defined as

$$C(r) = \langle \vec{S}_0 \cdot \vec{S}_r \rangle = \langle S_0^x \cdot S_r^x \rangle + \langle S_0^y \cdot S_r^y \rangle + \langle S_0^z \cdot S_r^z \rangle. \quad (3)$$

Figures 6(a) and 6(b) present the spin correlations $C(r)$ on the 80-site XC-cluster along the paths P-1 and P-2 (cf. Appendix D for reference). Since the path P-1 is considered along the alternating AFM $J - J'$ chain, the spin correlations in all three phases mentioned above exhibit short-range AFM correlation with exponential decay. On the other hand, the spin correlations along path P-2 show different behavior in different phases. We note that this path includes the subleading FM exchange J_d . In phase I, correlations indicate FM long-range order ($m_{\text{FM}} \approx 0.08$), while in phase III, a short-range AFM correlation with exponential decay is observed. The AFM correlations in phase III, however, decay faster than those of path P-1. However, in phase II, correlations vanish even at the next-nearest neighbor, which suggests that spins are highly disordered in this phase.

The spin correlations on the 80-site YC-cluster along the path P-1 (cf. Appendix D), which includes the subleading FM exchange J_c , are shown in Fig. 6(c). In phase I and phase III, correlations exhibit short-range AFM order with exponential decay and FM long-range order ($m_{\text{FM}} \approx 0.05$), respectively. This is opposite to that found for the path P-2 in XC geometry. However, in phase II, similar to path P-2 in the XC-cluster, the spin correlations vanish at the next-nearest neighbor.

The findings of spin correlation calculations are summarized in Table I. As is evident, phase I, characterized by a strong J_d , exhibits short-range AFM correlation both in the $J - J'$ (X) as well as the J_c (Y) direction, which makes the correlation along J_d ferromagnetic with long-range order. In phase III, characterized by a strong J_c , on the other hand, correlation is of an AFM nature in the $J - J'$ (X-direction) and J_d (diagonal) directions, making the correlation along J_c FM. On the other hand, in phase II, with comparable values of J_c and J_d , the spins are disordered along both J_c and J_d with short-range AFM correlation along the leading $J - J'$ chain direction. This suggests a staggered and stripy spin orientation

TABLE I. Characterization of three different phases, based on the analysis of spin correlation, presented in Sec. VI B.

Path	Phase I (Staggered)	Phase II (Disorder)	Phase III (Stripy)
XC P-1 (along X-direction) (J - J' chain)	AFM order (short-range)	AFM order (short-range)	AFM order (short-range)
XC P-2 (along diagonal direction) (J_d chain)	FM order (long-range)	Nearest-neighbor correlation [$C(r) = 0$ for $r > 1$]	AFM order (short-range)
YC P-1 (along Y-direction) (J_c chain)	AFM order (short-range)	Nearest-neighbor correlation [$C(r) = 0$ for $r > 1$]	FM order (long-range)

in phase I and phase III, respectively. In phase II, where both subleading terms are comparable ($J_c \approx J_d$), the system experiences significant frustration in terms of fierce competition between J_c and J_d . This results in vanishing correlations along the Y and diagonal directions, leading to what we term the “disorder” phase. It is worth noting that in this “disorder” phase, however, there exists weak short-range order along the X-direction due to the presence of weakly alternating AFM chains.

Armed with information on spin correlations, which characterizes three different phases, we construct the zero-field phase diagram of this model, as shown in Fig. 7, in the parameter space of J_c/J and J_d/J for fixed $J'/J = 0.92$ based on the energy derivative. The local spin orientations in the *staggered* phase (phase I) and the *stripy* phase (phase III) are also shown in the inset of the phase diagram (Fig. 7).

VII. EFFECT OF AXIAL MAGNETIC FIELD

Upon clarification on the nature of the GS in the absence of any external perturbation, the next interesting question is, what is the effect of an external magnetic field on the GS of the Hamiltonian in Eq. (2)? In the “disorder” phase, the lowest singlet-triplet (ST) gap [$E_m = E(S^z = 1) - E(S^z = 0)$] is found to be finite, though the gap value is found to vary within the phase space of phase II. The gap value is found to be largest along the $J_c = J_d$ line and decreases upon moving away from this line. For fixed choice of $J'/J = 0.92$, the gap value for $J_c/J = -0.3$ and $J_d/J = -0.3$ is found to be ≈ 0.2 J while it reduces to ≈ 0.05 J for $J_c/J = -0.3$ and $J_d/J = -0.5$.

We note that at the $J_c = J_d$ point, due to the competing nature of J_c and J_d , they compensate. This results in a system that can be mimicked by decoupled alternating chains with a finite ST gap. This can be appreciated by considering the fact that the spin gap for a weakly dimerized chain is given by $\Delta(\delta) = A\delta^\beta$, where δ is dimerization, connected to the alternation ratio by the relationship $J'/J = \frac{1-\delta}{1+\delta}$ and $A = 2.0375$, $\beta = 0.7475$ [50]. Setting $J'/J = 0.92$ yields a value of 0.189 J, very close to our estimate of ~ 0.2 J for the case of $J_c = J_d$. Moving away from the $J_c = J_d$ line, which is the compensation point, the resultant uncompensated subleading interactions suppress the gap value from the single chain limit. The estimated value of 0.05 J for $J_c/J = -0.3$ and $J_d/J = -0.5$ is very close to the experimental estimate of 2 K for the compound and is

also supported by the DFT estimates of exchanges. Thus the spin gap can be reproduced either by considering a single alternating chain with an alternation parameter of 0.98, as employed in susceptibility fitting [14], or by considering a stronger alternation parameter of ~ 0.92 as found in the DFT study, but including uncompensated subleading interactions. The latter scenario turns out to be the realistic representation. The nonuniqueness of the fitting process of the susceptibility fit is demonstrated in Sec. IX. In comparison to the DFT, the estimate of J'/J is found to be robust, consistently obtained in a large number of solutions. It should be stressed that the effect of subleading interactions, either compensated or uncompensated, will be manifested in the excited-state properties. This would enable the difference between a single alternating chain model, as invoked in Ref. [14], and the interchain coupled chain model of the discussed system. This will be taken up in the following section.

The system size dependence of the spin gap is shown in the SM [45]. This shows that a gapped solution in the disorder phase survives even in the asymptotic limit [see Fig. 3(a) in the SM]. The gap can be closed at a critical field $B = B_{c1}$. For the parameters $J_c = -0.3$ and $J_d = -0.5$, the critical field is found to be ≈ 1.8 T, close to the experimentally found gap of ≤ 2 T [14]. However, in the staggered and stripy phases, the dominant ferromagnetic J_d and J_c lead to ordering along the diagonal and Y-direction, respectively, which result in the closing of the spin gap upon extrapolation to infinite size (see the SM [45]).

To understand the magnetization processes, we further computed the magnetization as a function of B . The results for the staggered and stripy phases are shown in Fig. 8(a), and that for the disordered phase is shown in Fig. 8(b). The results for the 20×4 lattice in XC geometry reveal that while in the staggered and stripy phases the magnetization $M = S_{\text{total}}^z = \sum_i S_i^z$ increases with B in steps of $\Delta S_{\text{total}}^z = 1$, in the disordered phase the magnetization (M) changes in steps of $\Delta S_{\text{total}}^z = 4$. Interestingly, throughout phase II, M changes in steps of $\Delta S_{\text{total}}^z = 4$, as in seen in Fig. 8(b) for a range of J_d/J values of -0.25 , -0.3 , and -0.5 , although the critical field for closing the gap varies. To probe this further, we carried out calculations on a (20×6) -site system in XC geometry, thereby increasing the system along the J_c bond direction, and focusing on the disordered phase with $J_d/J = -0.3$. We notice that while the critical field B_{c1} for the 20×4 and 20×6 XC clusters remains nearly the same

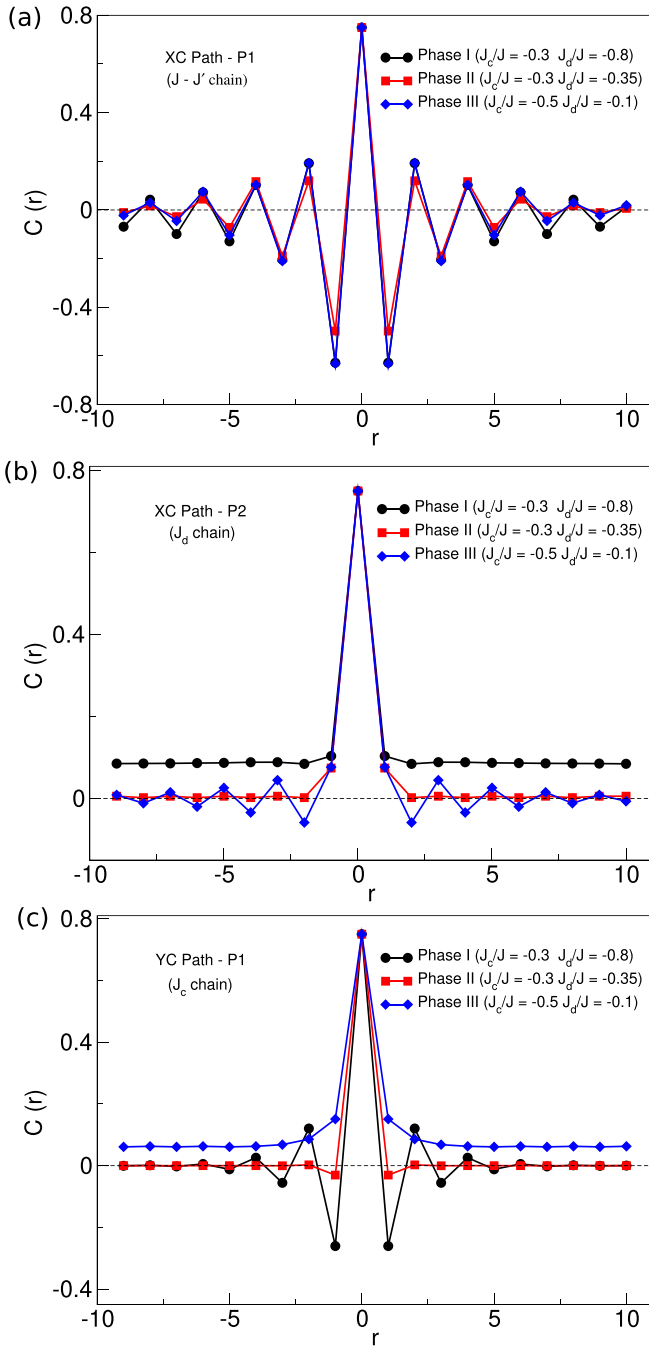


FIG. 6. Correlations $C(r)$, computed for different paths and geometries in the DMRG calculation (see Appendix D) in three different phases: (a) along path P-1 in XC geometry, (b) along path P-2 in XC geometry, and (c) along path P-1 in YC geometry.

($\approx 0.2J$), the magnetization changes in steps of $\Delta S_{\text{total}}^z = 6$ in comparison to 4, as found in a (20×4) -site system. Thus, the magnetization step scales with the system size along the J_c bond direction, signaling multimagnon condensation in phase II. We call this phenomenon magnon condensation, as the quasiparticles generated in the weakly dimerized chains are identified as magnons [51]. The magnons on each leg develop attractive interactions with the magnons on the neighboring chains. Consequently, a multimagnon condensate is formed

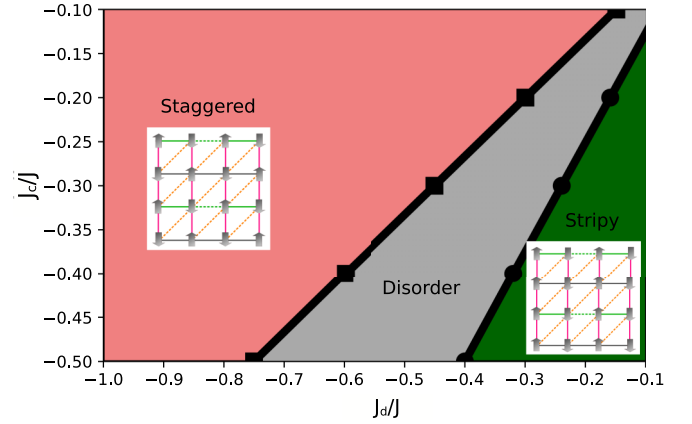


FIG. 7. Phase diagram of the 2D effective model Hamiltonian \mathcal{H} in Eq. (2) in parameter space of J_d/J and J_c/J , constructed out of ED total energy and DMRG computed spin correlations. The inset shows the local spin orientations in the *staggered* and *stripy* phases.

in a finite field that regulates the magnon density within the system.

VIII. MULTIMAGNON CONDENSATION

In the multimagnon condensation phase, a large number of magnons form a bound state, and there are two quantities to characterize this phase. The first is the order parameter, which is discussed in Appendix E, and the second is the binding energy of the bound state. We computed the binding energy of an n -magnon condensed state [23,24]. The per magnon binding energy of an nn -magnon bound state can be defined as

$$E_b(n) = \frac{1}{n} \{ [E(S^z - n) - E(S^z)] - n[E(S^z - 1) - E(S^z)] \}, \quad (4)$$

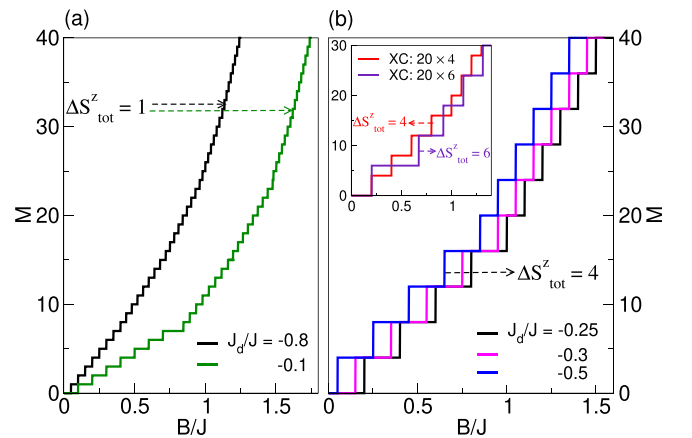


FIG. 8. DMRG computed magnetization in XC geometry with system size 20×4 in (a) staggered and stripy phase, (b) disorder phase plotted as a function axial magnetic field. In all the calculations, J'/J and J_c/J are fixed at 0.92 and -0.3 , respectively. J_d/J values are chosen to be -0.8 , and -0.1 in (a) and -0.25 , -0.3 , and -0.5 in (b). The inset in (b) shows the system size dependence of magnetization in disorder phase, shown for the representative case of $J_d/J = -0.3$.

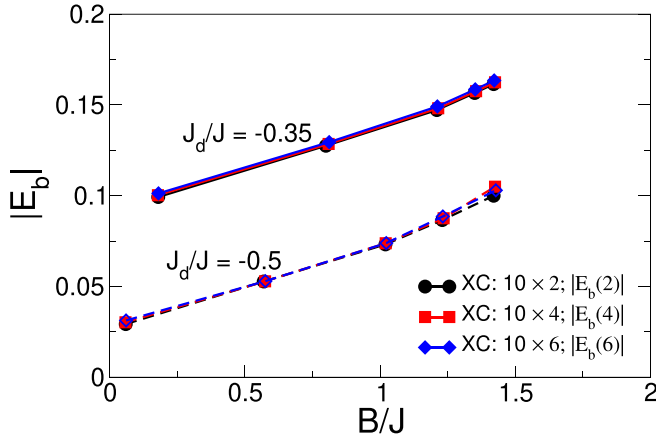


FIG. 9. DMRG computed absolute value of the binding energy per magnon $[|E_b(n)|]$ as a function of external magnetic field (B/J) for 10×2 , 10×4 , and 10×6 system sizes in XC geometry. The parameters of the spin model are chosen to belong to the disorder phase with a choice of $J_d/J = -0.35$, -0.5 for fixed $J'/J = 0.92$, $J_c/J = -0.3$.

where $E(S^z = S)$ is the GS energy in the $S^z = S$ sector. For stabilization of the n -magnon condensed state, the corresponding binding energy $E_b(n)$ should be negative. We computed the binding energy of two-magnon, four-magnon, and six-magnon states in the disordered phase in 10×2 , 10×4 , and 10×6 XC geometry for the representative cases of $J_d/J = -0.35$ and -0.5 , with fixed $J'/J = 0.92$ and $J_c/J = -0.3$ values. Figure 9 shows the plot of $|E_b(n)|$ as a function of the external magnetic field B/J . We find that the magnitude of binding energy increases with the magnetic field, suggesting increased stabilization of a multimagnon bound state with increasing field strength. The binding energy is found to be maximum at $J_c = J_d$ when the system is highly frustrated, and it decreases away from the $J_c = J_d$ line.

The finite binding energy indicates a multimagnon condensed state, which can be rationalized as follows. The ground state of the disordered phase exhibits a singlet state characterized by short-range AFM correlations along the J - J' chain, while only a weak nearest-neighbor ferromagnetic correlation persists along the Y and diagonal directions. To understand the attractive nature of the magnon, we use the mean-field approximation for weak subleading exchange interactions J_c and J_d . In this limit, these subleading terms act as an effective magnetic field generated by the magnetic moments on neighboring chains, and the field strength is proportional to J_c and J_d . The mean-field model Hamiltonian is the sum over all J - J' spin-1/2 chains under the effective field of the magnetic moments of other neighboring chains, and the external magnetic field B and the Hamiltonian can be expressed as

$$\mathcal{H}_{\text{MF}} \equiv \sum_i \sum_j J \vec{S}_{i,j} \cdot \vec{S}_{i+1,j} + J' \vec{S}_{i+1,j} \cdot \vec{S}_{i+2,j} - \vec{B}_{\text{eff}}(J_c, J_d, B) \cdot \vec{S}_{i,j}, \quad (5)$$

where $\vec{S}_{i,j}$ represents the spin at the i th site of the j th effective single J - J' chain model, and J and J' are effective exchange interactions of dimerized chains. The total effective

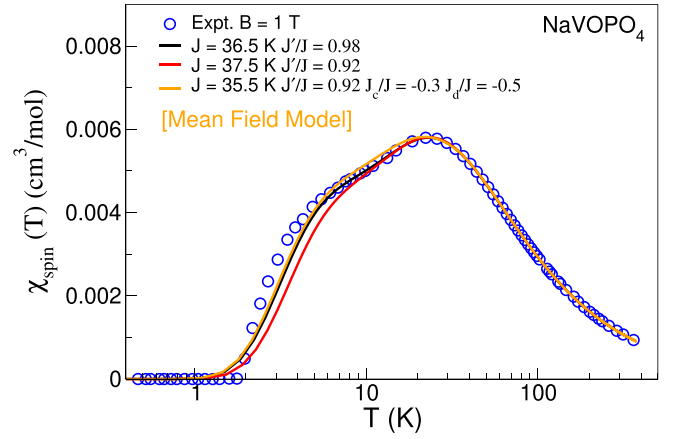


FIG. 10. Magnetic susceptibility of NaVOPO_4 in an applied field of 1 T, subtracting the impurity contribution. The experimental data are reproduced from Ref. [14]. The theoretically computed susceptibilities for various models are compared.

field, B_{eff} , is given by $[B - J_c(\langle \vec{S}_i, j+1 \rangle + \langle \vec{S}_i, j-1 \rangle) - J_d(\langle \vec{S}_{i+1, j+1} \rangle + \langle \vec{S}_{i-1, j-1} \rangle)]$, where B is the external field and $\langle \vec{S}_{i,j} \rangle$ is the average magnetic moment generated in the 2D model at the site with coordinates (i, j) at field B . We notice that both ferromagnetic interactions J_c and J_d induce an effective field that aligns the i th spin along the moment of the neighboring spin, i.e., they induce attractive interactions between the magnons on the neighboring chains.

Our analysis thus highlights the importance of the subleading ferromagnetic exchanges J_c/J and J_d/J in the stabilization of the multimagnon condensed phase. The presence of these two subleading interactions helps the process in two ways. First, the presence of competing J_c and J_d causes frustration, which significantly reduces the correlation length along the Y and diagonal directions. Second, the ferromagnetic subleading exchanges between the chains give rise to a finite binding energy between the magnons on different chains, acting as a glue for the multimagnon condensation.

IX. CALCULATED THERMODYNAMIC PROPERTIES: COMPARISON TO EXPERIMENTAL MEASUREMENTS

We next compute the measurable thermodynamic properties, taking into account the subleading interchain interactions, treated in a mean-field manner, and we compare with the published literature [14].

For this purpose, we first compute the magnetic susceptibility. The comparison of different models with experimentally measured susceptibility [14] in the presence of the magnetic field of 1 T after subtracting the impurity contribution is shown in Fig. 10. As is seen from the plot, an equally good fit of the measured susceptibility can be obtained either by a 1D alternating chain model with an alternation parameter of 0.98, or by a model including subleading interchain interactions with a slightly stronger alternation parameter of 0.92, upon a slight variation in value of J (36.5 versus 35.5 K).

We also compute the specific heat and compare it with the experimental data from Ref. [14] at zero magnetic field

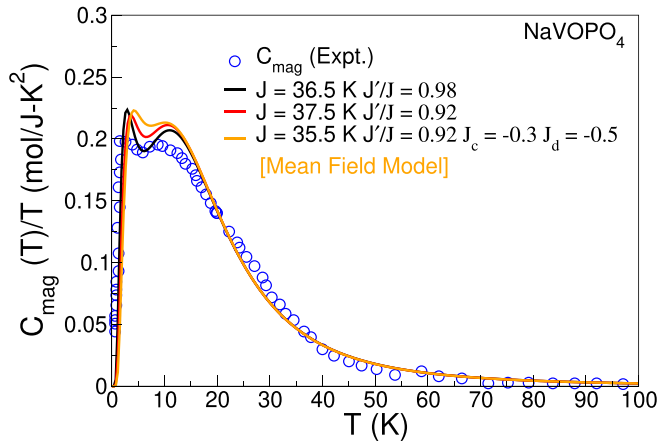


FIG. 11. Magnetic contribution of the specific heat. The theoretically computed results for various models are compared with the experimental data from Ref. [14].

(Fig. 11). It should be noted that the measured specific heat always has a dominating phonon contribution, and subtraction of the phonon contribution is not straightforward. We consider the magnetic contribution of specific heat as published in Ref. [14]. The 1D alternating chain model and our proposed model produce comparable results.

X. THE MATERIALS PERSPECTIVE—EFFECT OF STRAIN

Following the construction of a $J_c/J - J_d/J$ phase diagram, through a solution of the model spin Hamiltonian, it is a worthwhile exercise to put the material's perspective in it. Using the DFT-derived average value of parameters, as given in Table III, the positioning of NVOPO in the phase diagram is marked with the red symbol, while the box depicts the probable position taking into account the standard deviation in estimates of exchanges (cf. Table III). As is seen, the box falls in region II, characterized by multimagnon condensation, separated from the one-magnon state.

Considering the important effect of competing ferromagnetic couplings J_c and J_d in driving the multimagnon condensed phase, we next investigate the effect of uniaxial tensile strain applied along the c -axis in tuning these exchanges. The system was subject to 1–3 % tensile strain. The system was fully relaxed for the in-plane a and b lattice parameters, keeping the volume intact, and for the free atomic positions. As a first approximation, for a 3D solid without significant anisotropy, the assumption of fixed volume is expected to hold well, especially for uniaxial strain. We have explicitly checked this by carrying out relaxation without the constraint of constant volume. The fixed-volume constraint is found to have a minimal effect, with the lattice parameters and the free atomic positions differing by less than 1%.

The application of strain is found to affect mostly the structural parameters related to V-V chains running along the c -axis. In particular, for 1% and 3% tensile strain, 1NN V-V bond length is found to change from 3.56 Å to 3.60 Å to 3.70 Å, while the V-O-V bond-angle is found decrease slightly from 144.9° to 144.8° to 144.2°.

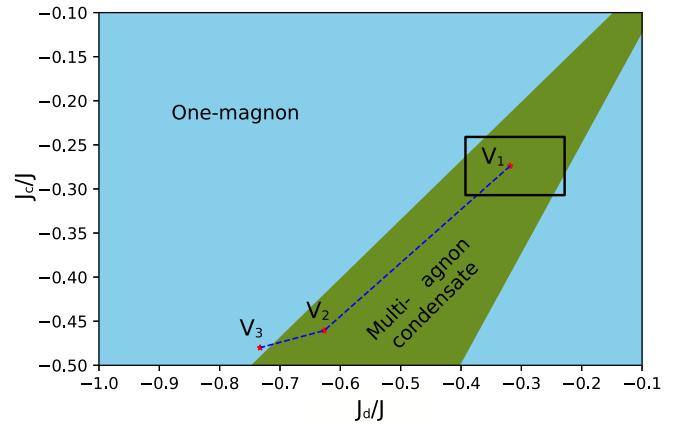


FIG. 12. Phase diagram: $J_c/J - J_d/J$ phase diagram divided into multimagnon condensed phase (marked in green) and the one-magnon, dipolar phase (marked in light blue). The data-point marked as V1 represents the positioning of NVOPO in the phase diagram, based on DFT estimates of the average value of exchanges. The box represents the positioning taking into account the standard deviations in DFT estimated exchanges. The data points V2 and V3 show the positioning upon application of 1% and 3% tensile uniaxial strain along the c -axis, respectively.

The structural changes upon application of 1% strain resulted in an increase in the average value of J_c by 67.5%, a decrease in J_d by 30.24%, and thus increments in J_d of 116.11% compared to the corresponding average J values in an unstrained condition. Interestingly, the alternation parameter α was found to remain more or less unchanged. Thus, application of 1% strain, as seen in Fig. 12, pushes the system deeper into the disordered phase. A further increase of the strain value to 3% increases the J_c with a substantial increase in J_d , thus driving a quantum phase transition from a gapped to a gapless state.

XI. SUMMARY AND DISCUSSION

The physics of quantum spin chain compounds has been discussed at length in the literature. The NaVOPO₄ compound, in this context, has been recently studied experimentally by x-ray diffraction, magnetic susceptibility, high-field magnetization, specific heat, electron spin resonance, as well as nuclear magnetic resonance measurements [14]. The fit of susceptibility resulted in a $J - J'$ model with an extremely weak alternation parameter α of 0.98 [14], in agreement with an estimated spin gap value of 2 K. The DFT study [14] indicated the possible presence of other subleading interactions. The effect of the subleading interactions in the description of the field-induced excited-state properties remains to be explored.

In our study, we first revisit the first-principles modeling of NVOPO. In this context, we extend beyond Ref. [14] through two complementary techniques: (a) application of the downfolding technique to define a low-energy three-orbital model Hamiltonian in an effective Wannier function basis, and (b) mapping of GGA+ U total energy to the spin model. The tight-binding representation of the low-energy Hamiltonian suggests that first, third, fourth, and eighth neighboring

hopping pathways are enough to capture the low-energy physics. Following this finding, we construct a minimal spin-Hamiltonian with four exchange integrals. We estimate the average values and the standard deviations of these four exchanges by solving a large number of equations ($\sim 11C_4$) obtained from GGA+ U total calculations of 12 different spin configurations. This led to a spin model with the hierarchy of exchange coupling, two major, similar AFM interactions, J and J' , as found previously [14], and two other subleading interactions, FM J_c and AFM J_d with $J_c > J_d$. This led to an intricate 3D spin model of a parallel array of $J - J'$ chains running along two perpendicular directions, in two consecutive ab planes, stacked along the c direction, connected by J_c and a body-diagonal interaction of J_d . Our rigorous first-principles modeling establishes a robust $J - J'$ alternation parameter of ~ 0.92 , and a large variation in the values of the two subleading interactions, dependent rather strongly on the chosen spin configuration.

The constructed spin model is solved using ED and DMRG. To make the problem numerically tractable, a 2D approximation of the full 3D model is used, with $J - J'$ AFM chains alternating with uniform AFM chains of $(J + J')/2$ exchanges, connected via an FM J_c and a renormalized FM exchange, J_d . The large variation in the DFT estimated values of subleading interchain interactions prompted us to construct a phase diagram in the parameter space of J_c and J_d . The constructed $J_c/J - J_d/J$ phase diagram with J'/J fixed at a DFT-derived value results in three distinct phases: two long-range ordered phases with staggered and stripy local spin orientations, and a spin-gapped *disorder* phase, characterized by short-range correlation along the $J - J'$ chain, and vanishing correlation along J_c and J_d . Our analysis brings out the competing nature of the two subleading interactions, J_c and J_d . This competing nature leads to a cancellation of interchain interactions at the $J_c = J_d$ line in the GS. The system thus can be represented as a collection of decoupled weakly dimerized chains having a finite spin gap. Away from the $J_c = J_d$ line, the gap is suppressed due to partial cancellation between J_c and J_d , and finally an ordered state prevails driven by the dominance of one competing interaction over the other. The computed spin gap value for choices of J_c and J_d in the disordered phase agrees well with the experimentally measured value. The calculated thermodynamic properties, such as magnetic susceptibility and specific heat, also provide a faithful representation of the experimental data [14].

The disorder phase, stabilized by comparable values of competing interactions J_c and J_d , as opposed to that of a single alternating dimerized chain, is found to host a multimagnon condensed phase upon gap closing by a critical magnetic field. The competing subleading exchanges J_c and J_d are found to play a key role in driving the observed field-induced multimagnon condensation state by providing the glue to the magnetic field generated magnons on different chains [25–27]. In contrast to the dipolar XY order in the BEC [20], the multimagnon condensed phase exhibits finite multimagnon binding energy and hosts multipolar order [26,29,30]. We computed the multipolar order parameter and found it to be finite in the multimagnon condensed phase. Note that, very recently, the Tomonaga-Luttinger-liquid physics of NVOPO was studied experimentally [52]. This is a finite-temperature

phase, with a temperature scale above the scale of interchain interactions. Our focus is the low- T behavior, below the scale of subleading interactions J_a (J_d) and J_c , that leads to the condensed phase rather than the liquid phase.

A transition from a gapful to a gapless state is envisaged upon the application of moderate-strength uniaxial strain, driving a quantum phase transition. We further note that among the class vanadate compounds with chainlike structures, NVOPO is unique due to the weak nature of the alternation. The underlying physics upon application of a magnetic field is expected to be different for AgVOAsO₄ [11] or NaVOAsO₄ [13] with a significantly stronger alternation ratio of ~ 0.6 , and thus stronger dimerization. In particular, the scenario of multimagnon condensation in the disorder phase proposed in the present study relies on the phenomena of weak dimerization where magnons from each $J - J'$ chain generate an n -magnon bound state. Note that the observed disorder phase in the present system arises due to frustration in the system, not because of the dimerization. This scenario is thus expected to change in the presence of strong dimerization. A detailed study on this will be taken up in the future.

Finally, while the studied 2D model was devised to overcome the numerical restrictions, motivated by the electronic aspects of NVOPO, it will, in general, be important in understanding the physics of the 2D frustrated model with possible implications to various gapped quantum magnets. In particular, the stabilization of the multimagnon condensed phase, driven by the frustration in weakly dimerized systems, will be of potential interest to the community.

ACKNOWLEDGMENTS

M.G. acknowledges CSIR, India, for the senior research fellowship [Grant No. 09/575 (0131) 2020-EMR-I]. M.R. acknowledges DST-India for financial help. M.K. acknowledges support from SERB (Grant sanction No. CRG/2020/000754). T.S.D. acknowledges JC Bose National Fellowship (Grant No. JCB/2020/000004) for funding.

APPENDIX A: THREE-ORBITAL MODEL

Table II lists the non-negligible hopping, connecting first-neighbor (1NN) (t_c), 3NN (t), 4NN (t'), and 8NN (t_a) V pairs. The on-site matrix elements show the presence of small off-diagonal elements due to angular distortion of O-V-O bond angles in the VO₆ octahedra.

APPENDIX B: DETAILS OF TOTAL ENERGY CALCULATIONS AND EXCHANGES

We consider a $3 \times 3 \times 1$ supercell, containing 36 V ions (cf. Fig. 13). There should thus be 2^{36} configurations of V-spins possible, out of which 12 were found to be independent (distinct), including the FM arrangement. This leads to 11 different energy differences, measured from FM energy, and thus 11 different equations with four unknown J 's. Choosing four out of 11 available equations leads to 330 possible sets of J values. Table III shows the spin arrangements, energy differences, and exchange values in four representative sets, obtained from GGA+ U calculations with $U = 4$ eV. We note that the U values estimated by linear response for vanadium

TABLE II. 3×3 on-site matrices and hopping integrals of the V t_{2g} only three-orbital model. The matrix elements are given in eV. Listed are also the J values in K, obtained employing the perturbative approach.

t_i	Bond-length (Å)	Connecting vector	d_{xy}	d_{yz}	d_{xz}	J_i (K)
On-site		[0.000, 0.000, 0.000]	$d_{xy} \begin{cases} -1.057 & 0.048 & -0.001 \end{cases}$	$d_{yz} \begin{cases} 0.048 & -0.432 & -0.018 \end{cases}$	$d_{xz} \begin{cases} -0.001 & -0.018 & -0.373 \end{cases}$	
$t_1 = t_c$	3.565	[0.000, -0.024, -0.421]	$d_{xy} \begin{cases} 0.000 & 0.043 & -0.007 \end{cases}$	$d_{yz} \begin{cases} -0.073 & -0.261 & 0.128 \end{cases}$	$d_{xz} \begin{cases} -0.031 & -0.152 & -0.075 \end{cases}$	-5.336
$t_3 = t$	5.337	[-0.354, 0.476, 0.216]	$d_{xy} \begin{cases} 0.089 & 0.014 & 0.009 \end{cases}$	$d_{yz} \begin{cases} -0.014 & 0.005 & -0.002 \end{cases}$	$d_{xz} \begin{cases} 0.009 & 0.002 & 0.003 \end{cases}$	91.212
$t_4 = t'$	5.385	[0.344, -0.524, -0.114]	$d_{xy} \begin{cases} 0.120 & -0.035 & 0.028 \end{cases}$	$d_{yz} \begin{cases} 0.035 & -0.003 & 0.003 \end{cases}$	$d_{xz} \begin{cases} 0.028 & -0.003 & 0.002 \end{cases}$	161.665
$t_8 = t_a$	5.952	[-0.698, -0.024, -0.091]	$d_{xy} \begin{cases} 0.048 & -0.002 & 0.003 \end{cases}$	$d_{yz} \begin{cases} 0.024 & 0.010 & -0.004 \end{cases}$	$d_{xz} \begin{cases} -0.002 & 0.004 & -0.000 \end{cases}$	25.120

oxides lie in a range of 4–5 eV [53]. In all the cases, J and J' turn out to be the dominant exchanges of antiferromagnetic nature of comparable magnitude, along with subleading exchanges, J_c and J_a , of an antiferro- and ferromagnetic nature, in agreement with the perturbative estimates. The average along with the percentage standard deviation of J values,

considering all the sets, are also shown in Table III. In addition to the estimates obtained from total energies calculated with $U = 4$ eV, those obtained with the choice of $U = 5$ eV are presented for comparison. The qualitative trend remains the same. This leads to a spin model of a three-dimensionally-coupled, weakly alternating spin chain.

TABLE III. The spin arrangements (cf. Fig. 13 for numbering of the V ions) with “+” and “-” denoting up and down spins, total energy difference ΔE , and exchange integral estimates for four representative sets. The bottom table lists the average values and standard deviation of J 's obtained from GGA+ U calculations with a choice of $U = 4$ and 5 eV, and Hund's coupling of $J_H = 1$ eV, as appropriate for 3d transition metal.

AFM <i>i</i>	1–8	9	10	11	12	13	14	15	16–19	20	21	22	23	24	25	26	27	28–36	ΔE (meV)
AFM1	+	+	+	+	-	+	+	-	+	+	+	+	+	+	+	+	+	+	-2.218
AFM2	+	-	-	-	+	+	+	+	+	+	+	+	+	+	+	+	+	+	-10.989
AFM3	+	+	+	+	+	+	+	+	+	-	-	-	+	+	+	+	+	+	-5.598
AFM4	+	+	+	+	+	+	+	+	+	+	+	+	+	+	-	-	-	+	-9.243
Set I: Exchange integral (K) $J = 45.77$, $J' = 42.30$, $J_c = -10.14$, and $J_a = 1.86$																			
AFM1	+	-	-	-	+	+	+	+	+	+	+	+	+	+	+	+	+	+	-10.989
AFM2	+	+	+	+	+	+	+	+	+	-	-	-	+	+	+	+	+	+	-5.598
AFM3	+	+	+	+	+	+	+	+	+	+	+	+	+	+	-	-	-	+	-9.243
AFM4	+	+	+	+	-	+	+	-	+	-	+	+	+	+	+	+	+	+	-1.730
Set II: Exchange integral (K) $J = 44.89$, $J' = 42.30$, $J_c = -10.14$, and $J_a = 2.30$																			
AFM1	+	+	+	+	-	-	-	+	+	+	+	+	+	+	+	+	+	+	-8.582
AFM2	+	+	+	+	+	+	+	+	+	+	-	-	-	+	+	+	+	+	-7.482
AFM3	+	+	+	+	+	+	+	+	+	+	+	+	-	-	-	+	+	+	-5.067
AFM4	+	+	+	+	-	+	+	-	+	-	+	+	+	+	+	+	+	+	-1.730
Set III: Exchange integral (K) $J = 43.20$, $J' = 40.78$, $J_c = -11.77$, and $J_a = 4.47$																			
AFM1	+	+	+	+	+	+	+	+	+	-	-	-	+	+	+	+	+	+	-5.598
AFM2	+	+	+	+	+	+	+	+	+	+	+	+	-	-	-	+	+	+	-5.067
AFM3	+	+	+	+	+	+	+	+	+	+	+	+	+	+	-	-	-	+	-9.243
AFM4	+	+	+	+	-	+	+	-	+	-	+	+	+	+	+	+	+	+	-1.730
Set IV: Exchange integral (K) $J = 44.89$, $J' = 42.30$, $J_c = -13.99$, and $J_a = 6.16$																			
U (eV)	J_H (eV)		J_c (K)			J (K)			J' (K)			J_a (K)							
4	1		$-12.17 \pm 12.56\%$			$44.51 \pm 2.07\%$			$40.59 \pm 2.41\%$			$4.71 \pm 31.34\%$							
5	1		$-11.13 \pm 11.02\%$			$36.33 \pm 2.03\%$			$32.84 \pm 2.38\%$			$3.89 \pm 30.30\%$							

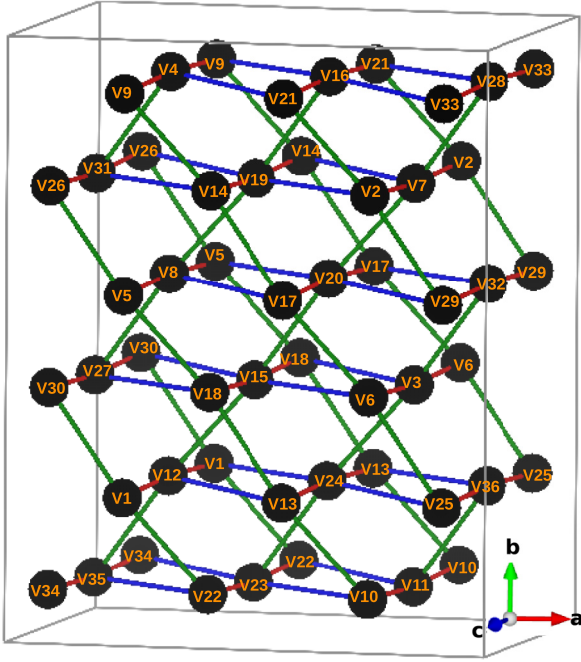


FIG. 13. $3 \times 3 \times 1$ supercell containing 36 V ions, employed for total energy calculations. The numbering of V atoms is used to represent the magnetic arrangements given in Table III. The V ions connected via J_c , J_a , and $J - J'$ are shown as magenta, blue, and green bonds, respectively.

APPENDIX C: CONSTRUCTION OF AN EFFECTIVE 2D MODEL FROM THE 3D MODEL

Construction of an effective 2D model from the 3D model involves a rotation of planes. As shown in Fig. 1(c), the alternating chains belong to two perpendicular planes, rotated by 90° with respect to each other, giving rise to a 3D character, even in the absence of the diagonal interaction, J_a , and the out-of-plane interaction, J_c . The 2D mapping of the 3D model containing two perpendicular planes of alternating chains is illustrated in Fig. 14. As is seen from the figure, the site V5 (marked in blue) is common between the two planes, i.e., the plane of 2D projection and the plane to be projected. The plane can be projected through clockwise [cf. panel (a)] and anticlockwise [cf. panel (b)] rotation, which maps sites V14 and V11 from the plane to be projected to sites V6 and V4 in the plane of 2D projection. The clockwise (anticlockwise) rotations connect V6 to V14 (V11) and V4 to V11 (V14). While in the 3D model, the site V5 is not connected to V4 and V6, in the effective 2D model, a J or J' bond is established following either clockwise or anticlockwise rotation. The resultant one, combining the two paths of rotation, is shown in panel (c) of the figure, where the site V5 gets connected to effective sites V6 and V4 via an average interaction $\frac{(J+J')}{2}$.

Finally, the frustration in a 3D model involving three AFM exchanges and an FM exchange, and that in an effective 2D model involving one AFM and two FM exchanges, is illustrated in Fig. 15. As is seen, frustration originates from J_a and J_c in the 3D model, while it originates from J_d in the 2D model. J_d is thus approximated as $J_a + \gamma J_c$, with a variational parameter γ . With $|J_c|$ (FM) two to four times larger than

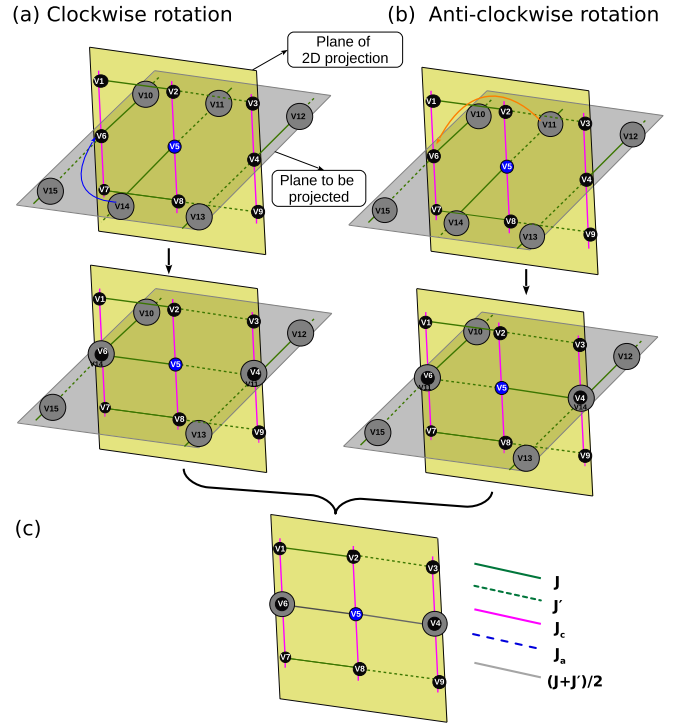


FIG. 14. Mapping of the 3D model of $J - J'$ chains to an effective 2D model. (a) Following clockwise rotation and (b) following anticlockwise rotation. The resultant 2D model is shown in (c).

$|J_a|$ (AFM), J_d is of FM nature, driving the frustration in the effective 2D model.

APPENDIX D: DMRG DETAILS

For DMRG calculations, we considered cylinders of two geometries XC and YC. In XC geometry, shown in Fig. 16(a), a periodic boundary condition (PBC) is applied along J_c bonds, while an open boundary condition (OBC) is applied along the $J - J'$ chain. This geometry enables the calculation of spin correlation along X ($J - J'$ chain direction) and diagonal (J_d chain direction) paths, P-1 and P-2, highlighted by green

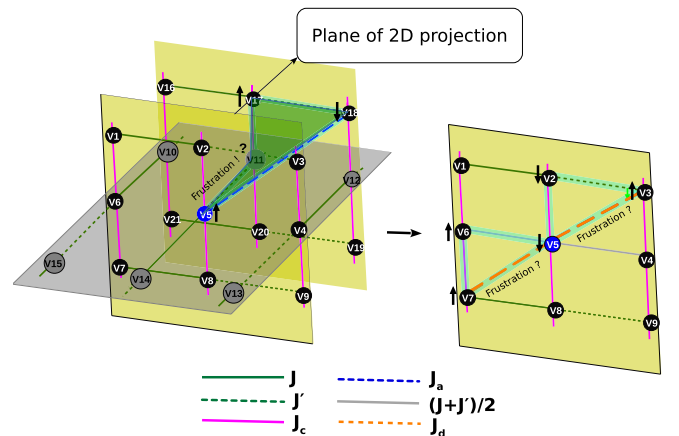


FIG. 15. Frustration effect in the 3D model (left) and in the effective 2D model (right).

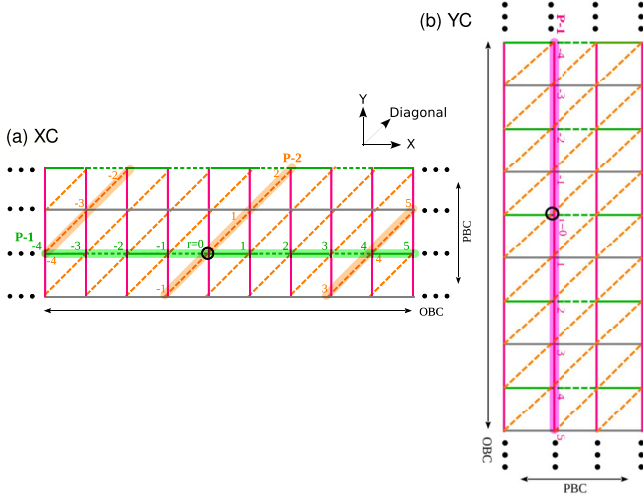


FIG. 16. XC/YC geometry used in DMRG calculations, as shown in (a)/(b) with PBC along Y/X and OBC along X/Y.

and orange lines in the figure. The YC geometry is a 90° rotation of the XC geometry, with the PBC along the J - J' chain and the OBC along J_c , as shown in Fig. 16(b). In this geometry, we consider only one path P-1 along the X-direction (J_c chain direction) highlighted by the magenta line.

APPENDIX E: MULTIPOLAR ORDER

In the presence of competing exchange interactions, magnons can bind together and form a bound state. In some cases, only two magnons pair up and form a quadrupolar state in the presence of an axial field [26,30], and they have the symmetric order parameter defined as $Q_{ij}^{x^2-y^2} = \frac{1}{2}(S_i^+ S_j^+ + S_i^- S_j^-)$, where S_i^+/S_j^- is a raising/lowering spin operator at site i/j . For a three-magnon bound pair, the order parameter is defined as $\hat{O}_{123} = (S_1^- S_2^- S_3^- + \text{H.c.})$. This order parameter can be generalized to an n -magnon bound state as

$$\hat{O}_{123\dots n} = (S_{i,1}^- S_{i,2}^- S_{i,3}^- S_{i,4}^- \cdots S_{i,n}^- + \text{H.c.}). \quad (\text{E1})$$

We notice that in Fig. 8(b) the step jump in the magnetization curve is proportional to the width of the 2D geometry. At the point of the jump, the GS state is twofold-degenerate, and the GS energies of the S^z and $S^z = n$ sectors are the same,

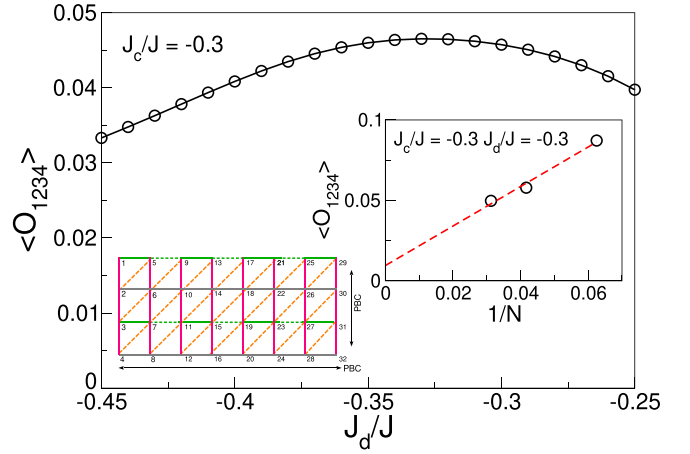


FIG. 17. Multipolar order parameter (\hat{O}_{1234}) as a function of J_d/J in the multimagnon condensed phase with system size 8×4 . In all the calculations, J'/J and J_c/J are fixed at 0.92 and -0.3 , respectively. The inset shows the system size dependence of multipolar order for the representative case of $J_d/J = -0.3$.

i.e., $E(S^z) = E(S^z + n)$. Therefore, the expectation value of $\hat{O}_{1234\dots n}$ can be calculated as an eigenvalue of the 2×2 matrix with elements $\langle \psi_\alpha | \hat{O}_{123\dots n} | \psi_\beta \rangle$, where $|\psi_{\alpha/\beta}\rangle$ are a GS wave function with spin multiplicity α/β , where α/β can take the value of S^z or $S^z + n$. Thus one can write the 2×2 matrix as

$$\hat{O}_{123\dots n} = \begin{bmatrix} \langle \psi_{S^z} | \hat{O}_{123\dots n} | \psi_{S^z} \rangle & \langle \psi_{S^z} | \hat{O}_{123\dots n} | \psi_{S^z+n} \rangle \\ \langle \psi_{S^z+n} | \hat{O}_{123\dots n} | \psi_{S^z} \rangle & \langle \psi_{S^z+n} | \hat{O}_{123\dots n} | \psi_{S^z+n} \rangle \end{bmatrix}, \quad (\text{E2})$$

where $\langle \psi_{S^z/S^z+n} | \hat{O}_{123\dots n} | \psi_{S^z/S^z+n} \rangle = 0$ and $\langle \psi_{S^z/S^z+n} | \hat{O}_{123\dots n} | \psi_{S^z+n/S^z} \rangle \neq 0$.

In this case, the order parameter for a system with a width of four sites along the J_c bond is $\hat{O}_{1234} = (S_{i,1}^- S_{i,2}^- S_{i,3}^- S_{i,4}^- + \text{H.c.})$, where S_i^- acts at site i along the J_c bond. We computed the order parameter (\hat{O}_{1234}) in the multimagnon condensed phase in 4×4 , 6×4 , and 8×4 toroidal geometries for fixed values of $J'/J = 0.92$ and $J_c/J = -0.3$. Figure 17 shows the plot of the order parameter (\hat{O}_{1234}) as a function of J_d/J for the 8×4 toroidal geometry. The J_d/J values were chosen over a range ensuring the system remains in the disordered phase. We find that the order parameter is maximum at $J_c/J = J_d/J$, where the four-magnon binding energy is also maximum. The inset of Fig. 17 shows the system size dependence of the order parameter (\hat{O}_{1234}). The system size dependence confirms that the order remains finite (~ 0.01) in the thermodynamic limit.

- [1] A. N. Vasil'ev, M. M. Markina, and E. A. Popova, Spin gap in low-dimensional magnets, *Low Temp. Phys.* **31**, 203 (2005).
- [2] S. Sachdev, Quantum criticality: Competing ground states in low dimensions, *Science* **288**, 475 (2000).
- [3] S. Sachdev, Quantum magnetism and criticality, *Nat. Phys.* **4**, 173 (2008).
- [4] S. Mukhopadhyay, M. Klanjšek, M. S. Grbić, R. Blinder, H. Mayaffre, C. Berthier, M. Horvatić, M. A. Continentino, A.

Paduan-Filho, B. Chiari, and O. Piovesana, Quantum-critical spin dynamics in quasi-one-dimensional antiferromagnets, *Phys. Rev. Lett.* **109**, 177206 (2012).

- [5] R. Chitra and T. Giamarchi, Critical properties of gapped spin-chains and ladders in a magnetic field, *Phys. Rev. B* **55**, 5816 (1997).
- [6] M. Klanjšek, H. Mayaffre, C. Berthier, M. Horvatić, B. Chiari, O. Piovesana, P. Bouillot, C. Kollath, E. Orignac, R. Citro,

- and T. Giamarchi, Controlling Luttinger liquid physics in spin ladders under a magnetic field, *Phys. Rev. Lett.* **101**, 137207 (2008).
- [7] B. Thielemann, C. Rüegg, K. Kiefer, H. M. Rønnow, B. Normand, P. Bouillot, C. Kollath, E. Orignac, R. Citro, T. Giamarchi, A. M. Läuchli, D. Biner, K. Krämer, F. Wolff-Fabris, V. Zapf, M. Jaime, J. Stahn, N. B. Christensen, B. Grenier, D. F. McMorrow, and J. Mesot, Field-controlled magnetic order in the quantum spin-ladder system $(\text{Hpip})_2 \text{CuBr}_4$, *Phys. Rev. B* **79**, 020408(R) (2009).
- [8] A. A. Aczel, Y. Kohama, C. Marcenat, F. Weickert, M. Jaime, O. E. Ayala-Valenzuela, R. D. McDonald, S. D. Selesnic, H. A. Dabkowska, and G. M. Luke, Field-induced Bose-Einstein condensation of triplons up to 8 K in $\text{Sr}_3\text{Cr}_2\text{O}_8$, *Phys. Rev. Lett.* **103**, 207203 (2009).
- [9] T. Hong, Y. H. Kim, C. Hotta, Y. Takano, G. Tremelling, M. M. Turnbull, C. P. Landee, H.-J. Kang, N. B. Christensen, K. Lefmann, K. P. Schmidt, G. S. Uhrig, and C. Broholm, Field-induced Tomonaga-Luttinger liquid phase of a two-leg spin-1/2 ladder with strong leg interactions, *Phys. Rev. Lett.* **105**, 137207 (2010).
- [10] B. Willenberg, H. Ryll, K. Kiefer, D. A. Tennant, F. Groitl, K. Rolfs, P. Manuel, D. Khalyavin, K. C. Rule, A. U. B. Wolter, and S. Süllow, Luttinger liquid behavior in the alternating spin-chain system copper nitrate, *Phys. Rev. B* **91**, 060407(R) (2015).
- [11] A. A. Tsirlin, R. Nath, J. Sichelschmidt, Y. Skourski, C. Geibel, and H. Rosner, Frustrated couplings between alternating spin- $\frac{1}{2}$ chains in AgVOAsO_4 , *Phys. Rev. B* **83**, 144412 (2011).
- [12] F. Weickert, A. A. Aczel, M. B. Stone, V. O. Garlea, C. Dong, Y. Kohama, R. Movshovich, A. Demuer, N. Harrison, M. B. Gamza, A. Steppke, M. Brando, H. Rosner, and A. A. Tsirlin, Field-induced double dome and Bose-Einstein condensation in the crossing quantum spin chain system AgVOAsO_4 , *Phys. Rev. B* **100**, 104422 (2019).
- [13] U. Arjun, K. M. Ranjith, B. Koo, J. Sichelschmidt, Y. Skourski, M. Baenitz, A. A. Tsirlin, and R. Nath, Singlet ground state in the alternating spin- $\frac{1}{2}$ chain compound NaVOAsO_4 , *Phys. Rev. B* **99**, 014421 (2019).
- [14] P. K. Mukharjee, K. M. Ranjith, B. Koo, J. Sichelschmidt, M. Baenitz, Y. Skourski, Y. Inagaki, Y. Furukawa, A. A. Tsirlin, and R. Nath, Bose-Einstein condensation of triplons close to the quantum critical point in the quasi-one-dimensional spin- $\frac{1}{2}$ antiferromagnet NaVOPO_4 , *Phys. Rev. B* **100**, 144433 (2019).
- [15] K. Lii, C. Li, T.-M. Chen, and S. Wang, Synthesis and structural characterization of sodium vanadyl (IV) orthophosphate NaVOPO_4 , *Z. Kristallogr.* **197**, 67 (1991).
- [16] L. Benhamada, A. Grandin, M.-M. Borel, A. Leclaire, and B. Raveau, Synthesis and crystal structure of a new vanadium IV phosphate: NaVOP sub 5, *C. R. Acad. Sci. Sér. 2* **314**, 585 (1992).
- [17] E. a. Iffer, M. Belaiche, C. A. Ferdi, M. Elansary, A. K. Sunar, Y. Wang, and Y. Cao, Monoclinic $\alpha\text{-NaVOPO}_4$ as cathode materials for sodium-ions batteries: Experimental and DFT investigation, *Int. J. Energy Res.* **45**, 1703 (2021).
- [18] V. Zapf, M. Jaime, and C. D. Batista, Bose-Einstein condensation in quantum magnets, *Rev. Mod. Phys.* **86**, 563 (2014).
- [19] T. Nikuni, M. Oshikawa, A. Oosawa, and H. Tanaka, Bose-Einstein condensation of dilute magnons in TiCuCl_3 , *Phys. Rev. Lett.* **84**, 5868 (2000).
- [20] T. Giamarchi, C. Rüegg, and O. Tchernyshyov, Bose-Einstein condensation in magnetic insulators, *Nat. Phys.* **4**, 198 (2008).
- [21] T. Rice, To condense or not to condense, *Science* **298**, 760 (2002).
- [22] A. W. Garrett, S. E. Nagler, D. A. Tennant, B. C. Sales, and T. Barnes, Magnetic excitations in the $S = 1/2$ alternating chain compound $(\text{VO})_2\text{P}_2\text{O}_7$, *Phys. Rev. Lett.* **79**, 745 (1997).
- [23] S. Nishimoto, S.-L. Drechsler, R. O. Kuzian, J. Richter, and J. van den Brink, The effect of antiferromagnetic interchain coupling on multipolar phases in quasi-1D quantum helimagnets, *J. Phys.: Conf. Ser.* **400**, 032069 (2012).
- [24] S. Nishimoto, S.-L. Drechsler, R. Kuzian, J. Richter, and J. van den Brink, Interplay of interchain interactions and exchange anisotropy: Stability and fragility of multipolar states in spin- $\frac{1}{2}$ quasi-one-dimensional frustrated helimagnets, *Phys. Rev. B* **92**, 214415 (2015).
- [25] J. Sudan, A. Lüscher, and A. M. Läuchli, Emergent multipolar spin correlations in a fluctuating spiral: The frustrated ferromagnetic spin- $\frac{1}{2}$ Heisenberg chain in a magnetic field, *Phys. Rev. B* **80**, 140402(R) (2009).
- [26] T. Hikihara, L. Kecke, T. Momoi, and A. Furusaki, Vector chiral and multipolar orders in the spin- $\frac{1}{2}$ frustrated ferromagnetic chain in magnetic field, *Phys. Rev. B* **78**, 144404 (2008).
- [27] A. Parvej and M. Kumar, Multipolar phase in frustrated spin-1/2 and spin-1 chains, *Phys. Rev. B* **96**, 054413 (2017).
- [28] L. Kecke, T. Momoi, and A. Furusaki, Multimagnon bound states in the frustrated ferromagnetic one-dimensional chain, *Phys. Rev. B* **76**, 060407(R) (2007).
- [29] A. Parvej and M. Kumar, Degeneracies and exotic phases in an isotropic frustrated spin-1/2 chain, *J. Magn. Magn. Mater.* **401**, 96 (2016).
- [30] N. Shannon, T. Momoi, and P. Sindzingre, Nematic order in square lattice frustrated ferromagnets, *Phys. Rev. Lett.* **96**, 027213 (2006).
- [31] J. P. Perdew, K. Burke, and M. Ernzerhof, Generalized gradient approximation made simple, *Phys. Rev. Lett.* **77**, 3865 (1996).
- [32] P. E. Blöchl, Projector augmented-wave method, *Phys. Rev. B* **50**, 17953 (1994).
- [33] A. Tackett, N. Holzwarth, and G. Matthews, A projector augmented wave (PAW) code for electronic structure calculations, part II: *pwpaw* for periodic solids in a plane wave basis, *Comput. Phys. Commun.* **135**, 348 (2001).
- [34] J. Paier, R. Hirschl, M. Marsman, and G. Kresse, The Perdew-Burke-Ernzerhof exchange-correlation functional applied to the G2-1 test set using a plane-wave basis set, *J. Chem. Phys.* **122**, 234102 (2005).
- [35] S. L. Dudarev, G. A. Botton, S. Y. Savrasov, C. J. Humphreys, and A. P. Sutton, Electron-energy-loss spectra and the structural stability of nickel oxide: An LSDA+ U study, *Phys. Rev. B* **57**, 1505 (1998).
- [36] O. K. Andersen and T. Saha-Dasgupta, Muffin-tin orbitals of arbitrary order, *Phys. Rev. B* **62**, R16219(R) (2000).
- [37] O. K. Andersen and O. Jepsen, Explicit, first-principles tight-binding theory, *Phys. Rev. Lett.* **53**, 2571 (1984).
- [38] E. R. Davidson, The iterative calculation of a few of the lowest eigenvalues and corresponding eigenvectors of large real-symmetric matrices, *J. Comput. Phys.* **17**, 87 (1975).
- [39] E. R. Davidson and W. J. Thompson, Monster matrices: their eigenvalues and eigenvectors, *Comput. Phys.* **7**, 519 (1993).

- [40] C. W. Murray, S. C. Racine, and E. R. Davidson, Improved algorithms for the lowest few eigenvalues and associated eigenvectors of large matrices, *J. Comput. Phys.* **103**, 382 (1992).
- [41] S. R. White, Density matrix formulation for quantum renormalization groups, *Phys. Rev. Lett.* **69**, 2863 (1992).
- [42] S. R. White, Density-matrix algorithms for quantum renormalization groups, *Phys. Rev. B* **48**, 10345 (1993).
- [43] U. Schollwöck, The density-matrix renormalization group, *Rev. Mod. Phys.* **77**, 259 (2005).
- [44] M. Kumar, Z. G. Soos, D. Sen, and S. Ramasesha, Modified density matrix renormalization group algorithm for the zigzag spin- $\frac{1}{2}$ chain with frustrated antiferromagnetic exchange: Comparison with field theory at large J_2/J_1 , *Phys. Rev. B* **81**, 104406 (2010).
- [45] See Supplemental Material at <http://link.aps.org/supplemental/10.1103/PhysRevB.110.054441> for additional information about DFT and DMRG calculations.
- [46] K. I. Kugel' and D. I. Khomski, The Jahn-Teller effect and magnetism: transition metal compounds, *Sov. Phys. Usp.* **25**, 231 (1982).
- [47] V. V. Mazurenko, F. Mila, and V. I. Anisimov, Electronic structure and exchange interactions of $\text{Na}_2\text{V}_3\text{O}_7$, *Phys. Rev. B* **73**, 014418 (2006).
- [48] H. Das, U. V. Waghmare, T. Saha-Dasgupta, and D. D. Sarma, Electronic structure, phonons, and dielectric anomaly in ferromagnetic insulating double perovskite $\text{La}_2\text{NiMnO}_6$, *Phys. Rev. Lett.* **100**, 186402 (2008).
- [49] I. Živković, V. Favre, C. Salazar Mejia, H. O. Jeschke, A. Magrez, B. Dabholkar, V. Noculak, R. S. Freitas, M. Jeong, N. G. Hegde, L. Testa, P. Babkevich, Y. Su, P. Manuel, H. Luetkens, C. Baines, P. J. Baker, J. Wosnitza, O. Zaharko, Y. Iqbal, J. Reuther, and H. M. Rønnow, Magnetic field induced quantum spin liquid in the two coupled trillium lattices of $\text{K}_2\text{Ni}_2(\text{SO}_4)_3$, *Phys. Rev. Lett.* **127**, 157204 (2021).
- [50] M. Kumar, S. Ramasesha, D. Sen, and Z. G. Soos, Scaling exponents in spin- $\frac{1}{2}$ Heisenberg chains with dimerization and frustration studied with the density-matrix renormalization group, *Phys. Rev. B* **75**, 052404 (2007).
- [51] We prefer to describe the quasiparticles in our system as magnons rather than triplons. In the present case, as alternation is very weak, each of the weakly dimerized chains has a very small singlet-triplet gap and higher excitations forming a continuum. The resultant quasiparticles thus have a very well defined dispersion curve, even in the absence of interchain interactions. Therefore, the quasiparticle in the discussed case, following the spirit of the earlier papers [*Phys. Rev. Lett.* **77**, 3649 (1996); *Phys. Rev. B* **55**, 15048 (1997); **67**, 054414 (2003)], should be called a magnon.
- [52] S. S. Islam, P. K. Mukharjee, P. K. Biswas, M. Telling, Y. Skourski, K. M. Ranjith, M. Baenitz, Y. Inagaki, Y. Furukawa, A. A. Tsirlin, and R. Nath, Repulsive Tomonaga-Luttinger liquid in the quasi-one-dimensional alternating spin- $\frac{1}{2}$ antiferromagnet NaVoPo_4 , *Phys. Rev. B* **109**, L060406 (2024).
- [53] J. W. Bennett, B. G. Hudson, I. K. Metz, D. Liang, S. Spurgeon, Q. Cui, and S. E. Mason, A systematic determination of Hubbard U using the GBRV ultrasoft pseudopotential set, *Comput. Mater. Sci.* **170**, 109137 (2019).